Title: Stable Pom1 clusters form a glucose-modulated concentration gradient that regulates mitotic entry

Authors: Corey A.H. Allard, Hannah E. Opalko, and James B. Moseley*

Author Affiliations: Department of Biochemistry and Cell Biology
The Geisel School of Medicine at Dartmouth, Hanover, NH 03755
*Corresponding author
james.b.moseley@dartmouth.edu

Abstract: Control of cell size requires molecular size sensors that are coupled to the cell cycle. Rod-shaped fission yeast cells divide at a threshold size partly due to Cdr2 kinase, which forms nodes at the medial cell cortex where it inhibits the Cdk1-inhibitor Wee1. Pom1 kinase phosphorylates and inhibits Cdr2, and forms cortical concentration gradients from cell poles. Pom1 inhibits Cdr2 signaling to Wee1 specifically in small cells, but the time and place of their regulatory interactions were unclear. We show that Pom1 forms stable oligomeric puncta that dynamically sample the cell cortex. Binding frequency is patterned into a concentration gradient by the polarity landmarks Tea1 and Tea4. Pom1 puncta colocalize with Cdr2 nodes, forming a glucose-modulated inhibitory threshold against node activation. Our work reveals how Pom1-Cdr2-Wee1 operates in multiprotein clusters at the cell cortex to promote mitotic entry at a specific size that can be modified by nutrient availability.

Introduction:

Many cell types display a remarkable ability to maintain a constant size during rapid cycles of growth and division (Fantes and Nurse, 1977; Ginzberg et al., 2015; Jorgensen and Tyers, 2004; Lloyd, 2013). Such cell size control is a systems-level property that emerges from the integration of multiple size-dependent signal transduction pathways. Each signaling pathway is comprised of tunable biochemical parameters, including gene-expression and post-translational modifications such as protein phosphorylation (Alberghina et al., 2009). One major challenge in cell size research is to understand the biochemical mechanisms of signal transduction in each pathway, and what makes them size-dependent. These control systems can generate size homogeneity for a given cell type, but cell size is also an adaptable property. For example, nutritional cues and other environmental factors can alter cell size (Fantes and Nurse, 1977; Kelkar and Martin, 2015; Shiozaki, 2009; Yanagida Mitsuhiro et al., 2011). Thus, a second major challenge in cell size research is to understand how size-dependent signaling pathways respond to changes in cell metabolism and stress.

In eukaryotic cells, these signaling pathways lead to regulated activation of the conserved cyclin-dependent kinase Cdk1 (Harashima et al., 2013). Activated Cdk1 triggers mitotic entry and the cascade of events that lead to cell division (Gould and Nurse, 1989; Simanis and Nurse, 1986). The fission yeast *Schizosaccharomyces pombe* represents an excellent model system to study size-dependent signaling pathways that regulate Cdk1. Genetic screens performed in past decades have identified many conserved factors that regulate Cdk1, but how these factors form size-dependent signaling pathways remains less clear. Fission yeast cells have a simple geometry that facilitates cell size studies. These cylindrical cells maintain a constant cell width, and grow by linear extension during interphase (Fantes and Nurse, 1977; Moreno et al., 1989). A network of cell polarity proteins positioned at cell tips restricts growth to these sites and maintains proper cell morphology (Chang and Martin, 2009). As a result, cell length doubles in one cell cycle, and many aspects of cell geometry scale with this increase in cell length (Gu and Oliferenko, 2019; Neumann and Nurse, 2007). Recent studies used cell shape mutants to show that fission yeast cells primarily measure surface area, not

length or volume, for cell size control (Facchetti et al., 2019; Pan et al., 2014). A critical next step is to understand how signaling pathways that regulate Cdk1 might operate at the cell cortex in a size-dependent manner.

In all eukaryotes, Cdk1 activity is established by the opposing activities of the inhibitory protein kinase Wee1, and the counteracting phosphatase Cdc25 (Gautier et al., 1991; Gould and Nurse, 1989; Kumagai and Dunphy, 1991; Russell and Nurse, 1986, 1987; Strausfeld et al., 1991). In fission yeast, mutations in Wee1, Cdc25, and their upstream regulators lead to changes in cell size that correspond to changes in the signaling pathways. Separate mechanisms appear to link cell size with regulation of Wee1 versus Cdc25. For Cdc25, its cellular concentration increases through unknown mechanisms as cells grow during interphase (Keifenheim et al., 2017; Moreno et al., 1990). In contrast, the concentration of Wee1 remains constant during interphase, but it is progressively phosphorylated by the conserved inhibitory kinases Cdr1 and Cdr2 (Aligue et al., 1997; Breeding et al., 1998; Kanoh and Russell, 1998; Keifenheim et al., 2017; Lucena et al., 2017; Opalko and Moseley, 2017; Russell and Nurse, 1987; Wu and Russell, 1993; Young and Fantes, 1987). *cdr2* mutants fail to divide at a constant surface area, and instead dividing according to cell volume or length (Facchetti et al., 2019). This change suggests that Cdr2-Cdr1-Wee1 signaling underlies the primary size-sensing pathway that relates to surface area, while additional pathways related to volume and length are engaged in its absence. The localization of Cdr2, Cdr1, and Wee1 supports this model. Cdr2 forms punctate oligomeric structures called nodes that stably bind to the medial cell cortex, and recruits Cdr1 to these sites (Akamatsu et al., 2014, 2017; Guzmán-Vendrell et al., 2015; Martin and Berthelot-Grosjean, 2009; Morrell et al., 2004; Moseley et al., 2009). Wee1 localizes primarily in the nucleus and spindle-pole body, where it encounters Cdk1 to prevent mitotic entry (Masuda et al., 2011; Moseley et al., 2009; Wu et al., 1996). In addition, Wee1 transiently visits cortical Cdr1/2 nodes in bursts that lead to inhibition of Wee1 kinase activity (Allard et al., 2018). The frequency and duration of these Wee1 bursts at Cdr1/2 nodes increase approximately twenty-fold as cells double in size during interphase (Allard et al., 2018). This mechanism leads to size-dependent inhibition of Wee1 by a signaling pathway at the cell surface.

This size-dependent change in Wee1 bursting dynamics is encoded into the Cdr1-Cdr2-Wee1 pathway at two proposed levels. First, increased Wee1 bursting depends upon the doubling in number of Cdr1/2 nodes, which occurs as growth results in a doubling of cell surface area, but this increase is smaller than the magnitude of change in Wee1 bursting (~2-fold vs ~20-fold) (Allard et al., 2018; Deng and Moseley, 2013; Pan et al., 2014). Second, activation of Cdr2 increases as cells increase in size (Deng et al., 2014). Cdr2 kinase activity is required for Wee1 localization to nodes, and is controlled by the upstream kinase Pom1 (Allard et al., 2018; Moseley et al., 2009). Pom1 directly phosphorylates and inhibits the activation of Cdr2 (Bhatia et al., 2014; Deng et al., 2014; Kettenbach et al., 2015; Martin and Berthelot-Grosjean, 2009; Moseley et al., 2009). Pom1 also phosphorylates a separate set of sites on Cdr2 to disrupt oligomerization and membrane binding (Bhatia et al., 2014; Rincon et al., 2014). This regulation of Cdr2 by Pom1 changes the size dependency of Wee1 bursts. Specifically, the frequency and duration of Wee1 bursts at Cdr1/2 nodes increases, but only in small cells (Allard et al., 2018). Consistent with this defect, *pom1*Δ cells divide at a small size due to dysregulation of the Cdr2-Cdr1-Wee1 pathway (Bähler and Pringle, 1998; Bhatia et al., 2014; Martin and Berthelot-Grosjean, 2009; Moseley et al., 2009; Wood and Nurse, 2013). Taken together, these results suggest a size-dependent interaction between Pom1 and its substrate Cdr2. However, the location and timing of Pom1 interactions with Cdr2 have remained poorly defined.

Pom1 localizes in a spatial gradient that is enriched at cell tips, with a lower concentration at the medial cell cortex, where its substrate Cdr2 forms nodes (Bähler and Pringle, 1998; Bhatia et al., 2014; Martin and Berthelot-Grosjean, 2009; Moseley et al., 2009; Pan et al., 2014). Thus, the majority of Pom1 and Cdr2 molecules in a cell are spatially separated, raising the question of when and where they interact. Several lines of evidence suggest that the spatial distributions of Pom1 and Cdr2 are critical for the size-dependent signaling properties of this pathway, and suggest the lateral cell cortex as the key interface. For example, ectopic targeting of Pom1 to the medial cell cortex inhibits Cdr2 node formation and Cdr2-dependent cell size signaling (Martin and

94 Berthelot-Grosjean, 2009). Additionally, the Pom1 gradient is dissipated as part of a
95 cellular response to glucose deprivation, which leads to increased Pom1 concentration at
96 the lateral cortex where it delays mitotic entry (Kelkar and Martin, 2015). This result also
97 demonstrates that Pom1-Cdr2 signaling responds to environmental input to coordinate
98 cell size with nutrient availability. In this system, Pom1 functions analogously to an
99 intracellular morphogen, acting as a concentration-dependent and localization-controlled
100 inhibitor of Cdr2 nodes. However, levels of Pom1 at the medial cell cortex in wild-type
101 cells growing under steady state conditions are low, constant, and do not vary with cell
102 size (Bhatia et al., 2014; Pan et al., 2014). The mechanism by which Pom1 provides size
103 specific input to Cdr2 is unclear and requires analysis of their molecular dynamics at the
104 lateral cell cortex.
105
106 Past studies have led to a model for Pom1 gradient formation driven by the binding
107 and diffusion of individual Pom1 molecules in the plasma membrane (Hachet et al., 2011;
108 Saunders et al., 2012). Pom1 binds directly to anionic phospholipids at the cell cortex,
109 and these interactions are disrupted upon intramolecular autophosphorylation (Hachet et
110 al., 2011). Polarity factors including Tea1 and Tea4 are enriched at the cell tips by
111 microtubules, where they recruit the protein phosphatase 1 (PP1) Dis2, which
112 dephosphorylates Pom1 to promote membrane attachment specifically at the cell tip
113 (Hachet et al., 2011). Cortical Pom1 molecules are then thought to diffuse in the plane of
114 the membrane away from the tip, until multiple autophosphorylation events disrupt
115 membrane binding (Hachet et al., 2011; Hersch et al., 2015; Saunders et al., 2012). Tip-
116 concentrated Pom1 occludes Cdr1/2 node formation, restricting them instead to the
117 medial cell cortex (Martin and Berthelot-Grosjean, 2009; Moseley et al., 2009).
118 Intriguingly, dynamic clusters of Pom1 have also been observed and are proposed to form
119 by unstable oligomerization of molecules diffusing in the plane of the membrane (Hachet
120 et al., 2011; Saunders et al., 2012). These clusters are thought to form and decay rapidly,
121 temporarily sequestering Pom1 molecules and thereby slowing molecular diffusion rates
122 and reducing noise in the gradient (Saunders et al., 2012). These puncta represent nano-
123 scale pockets of increased Pom1 concentration, but whether these clusters contribute to
124 regulation of Cdr2 nodes is unknown.

Here, we use biochemical approaches in combination with quantitative TIRF and confocal microscopy to show that the Pom1 gradient itself is formed by these punctate clusters. Pom1 puncta are stable oligomers that bind and release the membrane with minimal lateral diffusion. The frequency of Pom1 puncta binding is higher at cell tips than on cell sides. Thus, the gradient is formed because the membrane-association frequency of Pom1 puncta is patterned along the long axis of the cell. A portion of Pom1 puncta in the medial cell cortex colocalize with Cdr2 nodes, and the ratio of Pom1 to Cdr2 at the medial cell cortex changes as a function of cell size. When glucose availability is restricted, Pom1 clusters redistribute to the medial cell cortex to prevent dramatic dysregulation of Wee1 bursts. Our work reveals that the Pom1-Cdr2-Wee1 signaling pathway is organized as a series of cortical clusters. The relative distribution of these clusters at the plasma membrane changes with cell size and glucose availability, thus relaying cell surface area to the core cell cycle machinery in a nutrient-controlled manner.

Results:

The Pom1 gradient is formed by transient cortical puncta

We sought to examine the molecular dynamics of Pom1-Cdr2 signaling at the cell cortex. As a starting point, we imaged Pom1 by TIRF microscopy, which selectively excites fluorophores near the coverslip. Pom1 was tagged at the endogenous locus with the bright and photostable fluorophore mNeonGreen (mNG). Surprisingly, along the lateral cell cortex Pom1-mNG was localized almost exclusively in discreet puncta, with no apparent diffuse signal **(Figure 1A)**. In images from a single time-point, Pom1 puncta formed a noisy concentration gradient **(Figure 1B)**. Time-averaging produced a smoother gradient dotted by occasional clusters, similar to the gradient observed by confocal microscopy **(Figure 1A-B)**. Similar results were obtained by confocal microscopy **(Figure S1A-H)**. Pom1 puncta were highly dynamic. They appeared on the lateral cortex with a frequency of ~2 puncta*$\mu m^{-2}s^{-1}$, and remained bound for less than 2 seconds on average **(Figure 1C,F,H)**. During this brief cortical attachment, Pom1 puncta exhibited minimal diffusion which lacked directionality, and instead appeared to diffuse randomly in sub-micron patches of cortex **(Figure 1C,G)**.

156

157 Similar puncta were previously observed by confocal microscopy, but they were
158 not thought to form the Pom1 concentration gradient *per se* (Hachet et al., 2011;
159 Saunders et al., 2012). Our findings suggested the distinct possibility that the cortical
160 gradient itself is comprised of dynamic puncta. To test this possibility, we needed to image
161 Pom1-mNG at cell tips, which are inaccessible to visualization using standard slide
162 preparation for TIRF microscopy because this region is outside of the TIRF illumination
163 field. Therefore, we performed "head-on" TIRF imaging of cell tips. Pom1-mNG localized
164 at cell tips almost entirely in puncta, similar to cell sides **(Figure 1D-E)**. We also used
165 "head-on" Airyscan confocal imaging to confirm that Pom1 localization in puncta at tips
166 was not an artifact of the TIRF approach **(Figure S1I)**, a conclusion also supported by
167 work using high resolution wide-field microscopy (Dodgson et al., 2013). Compared to
168 cell sides, Pom1 puncta appeared twice as frequently at cell tips but with a similar cortical
169 duration, again exhibiting minimal and non-directional diffusion away from their binding
170 site **(Figure 1F-H)**. Fluorescence intensity of individual puncta at cell tips and cell sides
171 were similar, although we detected a low number of brighter puncta at cell tips, likely
172 representing multiple diffraction-limited puncta **(Figure 1I, Figure S1I-K)**. From these
173 data, we conclude that the Pom1 gradient is formed by patterning the membrane binding
174 frequency of cortical puncta along the long axis of the cell, rather than by diffusion of
175 Pom1 molecules from the cell tips to the cell side.

176

177 ***In vitro* analysis shows Pom1 exists in large, stable puncta**

178 Past work suggested that Pom1 puncta assemble and disassemble at the cortex
179 through oligomerization of individual molecules diffusing in the plane of the membrane
180 (Saunders et al., 2012). However, our high-speed (20ms/frame) continuous TIRF videos
181 suggested that Pom1 puncta bind and release the cortex as a pre-formed unit **(Figure**
182 **S2A)**. Consistent with this possibility, we observed rare cell lysis events in which Pom1
183 puncta remained intact in extruded cytoplasm **(Figure 2A)**. This apparent stability while
184 removed from the plasma membrane led us to test the existence and properties of Pom1
185 puncta in detergent cell extracts. Using TIRF microscopy, we observed puncta of Pom1-
186 mNG in extracts made from Pom1-mNG cells, but not from untagged wild-type cells

187 **(Figure 2B)**. We next examined the size of these Pom1 puncta by velocity sucrose
188 gradient sedimentation. By fractionating detergent cell extracts from *pom1-3xHA* cells,
189 we found that most Pom1 exists in a large 60S complex, consistent with Pom1 puncta
190 observed in cells. Fractions 6-8 containing this peak were dialyzed and centrifuged on a
191 second sucrose gradient. These pooled fractions again sedimented at 60S, indicating that
192 they represent a stable complex **(Figure 2C-D, S2B-C)**.
193
194 Pom1 complexes present in detergent extracts resemble the cortical puncta
195 observed in cells. To test this connection further, we examined the membrane-binding
196 capacity of Pom1 complexes *in vitro* using artificial supported lipid bilayers (SLBs). Pom1-
197 mNG puncta were isolated by sucrose gradient centrifugation, incubated with fluid SLBs
198 on coverslips, and then imaged by TIRF microscopy **(Figure 2E, S2E).** In this cell free-
199 system, Pom1-mNG puncta bound and released SLB lipids with strikingly similar
200 dynamics as in cells **(Figure 2E-F)**. Dwell times were increased for the kinase-dead
201 mutant Pom1(K728R)-mNG, which was previously shown to increase cortical Pom1
202 levels in cells **(Figure S2D)** (Bähler and Pringle, 1998; Hachet et al., 2011). Collectively,
203 our TIRF microscopy and *in vitro* analysis of Pom1 puncta support a model whereby the
204 majority of cellular Pom1 protein is contained within discreet, highly-stable oligomers that
205 bind and release membranes with kinetics dictated by their catalytic activity in a geometric
206 pattern that resembles a concentration gradient.
207
208 Formation of clusters could represent an intrinsic property of Pom1 protein, or
209 alternatively might require additional cellular factors. To distinguish between these
210 possibilities, we expressed and purified GST-Pom1 from bacteria, and then performed
211 sucrose gradient centrifugation experiments on this recombinant protein. Recombinant
212 GST-Pom1 sedimented in a low molecular weight peak unlike Pom1 puncta from cells.
213 Remarkably, purified GST-Pom1 was assembled into a puncta-sized high molecular
214 weight complex by incubation with wild-type yeast detergent extract **(Figure 2G)**.
215 Complex formation was also induced by incubation of GST-Pom1 with *pom1*Δ cell
216 extracts, meaning that additional cellular factors drive this assembly process. **(Figure
217 2G).** Once assembled, Pom1 puncta are stable oligomeric complexes with intrinsic

218 membrane-binding properties that can be reconstituted *in vitro*. Additional cellular
219 regulatory proteins are likely to promote the binding of Pom1 puncta at cell tips, leading
220 to the spatial gradient.
221
222 **Polarity landmarks pattern cortical dynamics of Pom1 puncta to shape the gradient**
223 The key role of puncta in forming the Pom1 gradient led us to reexamine the role of
224 cell polarity landmark proteins Tea1 and Tea4. Both of these proteins localize at cell tips
225 and are required for proper Pom1 gradient formation (Hachet et al., 2011). However, past
226 studies have shown that Tea1 and Tea4 have distinct mechanistic roles: Tea4 is required
227 for localization of Pom1 to the cortex, whereas Tea1 is required for enrichment of cortical
228 Pom1 to the cell tip (Hachet et al., 2011). We first used sucrose gradient centrifugation to
229 test if either protein is required for assembly of Pom1 into stable biochemical complexes.
230 The sedimentation pattern of Pom1 puncta isolated from *tea1*Δ and *tea4*Δ cells in velocity
231 sucrose gradients is unchanged from wild-type cells, suggesting that neither Tea1 nor
232 Tea4 are required for assembly of Pom1 into stable biochemical complexes **(Figure 3A)**.
233 Rather, these regulators are likely to act downstream of puncta assembly.
234
235 We next tested the localization and dynamics of Pom1-mNG in *tea1*Δ and *tea4*Δ cells.
236 Past work showed that membrane bound Tea4 is both necessary and sufficient to
237 nucleate cortical Pom1 gradients, and this relationship is non-stoichiometric (Hachet et
238 al., 2011). We confirmed that Pom1 was absent from the cell cortex in confocal
239 micrographs of *tea4*Δ cells **(Figure 3B)**. Surprisingly, we did observe Pom1-mNG puncta
240 at the cortex of *tea4*Δ cells by TIRF microscopy **(Figure 3C)**. These binding events
241 occurred at lower frequency and had a shorter dwell time than in wild-type cells **(Figure**
242 **3C-E)**. Pom1-mNG puncta in *tea4*Δ cells were distributed evenly around the cell cortex
243 with no detectable enrichment at tips. These infrequent, transient binding events do not
244 result in accumulation of enough cortical Pom1 to be detected by confocal microscopy.
245 Their rapid and position-independent association with the cortex leads to the absence of
246 a cortical Pom1 gradient in *tea4*Δ cells.
247

248 In contrast, confocal micrographs of Pom1-mNG in *tea1*Δ cells confirmed even
249 distribution around the entire cell cortex **(Figure 3B)**. TIRF microscopy of *tea1*Δ cells
250 revealed that this distribution arises from Pom1-mNG puncta, which bound the cell cortex
251 at a frequency in between the tips versus sides of wild-type cells **(Figure 3C-D)**. The
252 duration of individual binding events was longer than in *tea4*Δ cells but shorter than in
253 wild-type cells **(Figure 3E, S3A)**. Thus, in *tea1*Δ cells Pom1 puncta bind at an
254 intermediate frequency and for an intermediate duration, when compared to wild type and
255 *tea4*Δ cells. These binding events are independent of spatial cues at the cell ends versus
256 cell sides, resulting in enrichment of cortical Pom1 but not a gradient. Thus, Tea1 and
257 Tea4 cooperate to promote localized membrane binding but not assembly of Pom1
258 puncta. These spatial cues pattern the frequency of Pom1 puncta cortical interaction
259 along the long axis of the cell.
260
261 **Pom1 puncta interact with Cdr2 nodes at the lateral cortex**
262 It has been unclear when and where Pom1 interacts with its inhibitory target Cdr2,
263 which localizes in cortical nodes positioned in the cell middle. Since Pom1 puncta appear
264 to bind throughout the medial cell cortex, we used simultaneous two-color TIRF
265 microscopy to test colocalization of Pom1 puncta and Cdr2 nodes. We observed
266 unambiguous overlap between Cdr2 nodes and some Pom1 puncta, as well as Pom1
267 puncta that bound to the cortex without encountering a Cdr2 node **(Figure 4A)**. Thus,
268 Pom1 puncta bind to the medial cortex in a stochastic pattern that can generate overlap
269 with Cdr2 nodes. These patterns of colocalization were apparent in both static images
270 and time-lapse movies **(Figure 4A-B)**. The frequency, dwell time, and displacement of
271 Pom1 cortical puncta were unaffected in *cdr2*Δ cells **(Figure S4A-DC)**. These data
272 suggest that Pom1 interacts with its inhibitory phosphorylation target Cdr2 when Pom1
273 clusters associate with Cdr2 nodes at the medial cell cortex.
274
275 Phosphorylation by Pom1 prevents activation of Cdr2 in small cells, thereby
276 contributing to cell size-dependent regulation of Wee1 and mitotic entry (Allard et al.,
277 2018). To place this pathway in the context of Pom1 puncta and Cdr2 nodes, we analyzed
278 how these structures accumulate and colocalize as cells grow. Intriguingly, the total

279 number of both Cdr2 nodes and Pom1 puncta detected in TIRF images all along cell sides
280 were equivalent for cells of a given size **(Figure 4C-D)**. The numbers of both structures
281 show a similar size-dependent doubling. We next restricted our analysis to a 2μm x 2μm
282 square ROI positioned at the cell middle, where Cdr2 nodes concentrate. The local
283 density of Cdr2 nodes in this region increased as a function of cell size, consistent with
284 past studies (Deng and Moseley, 2013; Pan et al., 2014). In contrast, the density of Pom1
285 puncta in this region was largely independent of cell size **(Figure 4E)**. In both TIRF and
286 confocal images, the concentration of Pom1 protein and Pom1 clusters decreased slightly
287 as cells increase in size, but this trend was dwarfed by the cell size-dependent increase
288 in Cdr2 node density **(Figure 4E, S4D)**. Thus, as cells grow larger, the ratio of Pom1 to
289 Cdr2 in the medial cell cortex changes to favor Cdr2 because the densities of these two
290 structures scale differently with cell size **(Figure 4G)**.
291
292 We next tested how this density scaling affects colocalization of Pom1 clusters and
293 Cdr2 nodes as cells grow. Due to the increasing density of Cdr2 nodes, we observed an
294 increased number of colocalized Pom1 clusters and Cdr2 nodes as cells increase in size
295 **(Figure SE-F)**. The increased colocalization, combined with the constant density of Pom1
296 clusters, means that there are less "free" Pom1 clusters as cells increase in size **(Figure**
297 **S4G)**. Perhaps more importantly, the number of "free" Cdr2 nodes increased as a function
298 of cell size **(Figure S4G)**. These free Cdr2 nodes are not occupied by an inhibitory Pom1
299 cluster, and thus have increased potential to promote mitotic entry by inhibiting Wee1. In
300 this manner, Pom1 sets an inhibitory threshold that must be overcome by an increase in
301 Cdr2 node density. The inhibitory threshold decreases slightly as cells grow, and
302 functions most effectively in small cells, where Pom1 was previously shown to inhibit
303 downstream signaling to Wee1 (Allard et al., 2018).
304
305 **Control of Pom1 puncta levels in the medial cell cortex**
306 Our results suggest that Pom1 sets an inhibitory threshold that can be tuned by
307 altering the concentration of Pom1 cortical clusters in the cell middle. We sought to test
308 this model by increasing the abundance of Pom1 clusters in the cell middle. Low glucose
309 media and *tea1*Δ are two independent conditions that disperse Pom1 throughout the

310 cortex, thereby increasing its concentration in the cell middle (Hachet et al., 2011; Kelkar
311 and Martin, 2015) (See also **Figure S7A-C**). As a starting point, we tested the effect of
312 mislocalized Pom1 in *tea1*Δ cells **(Figure 5A-B)**. Surprisingly, higher Pom1 levels at the
313 medial cortex did not impact the number of Cdr2 nodes or their recruitment of Wee1
314 **(Figure 5C-F)**. Past work showed that Pom1 retains kinase activity in *tea1*Δ cells (Bähler
315 and Nurse, 2001), but several experiments suggested that this residual activity may be
316 reduced. First, we compared *in vitro* kinase activity of Pom1 immunoprecipitated from
317 *tea1*Δ cells or wild type cells. Pom1 from *tea1*Δ cells showed less kinase activity towards
318 itself (autophosphorylation) and its substrate Cdr2 **(Figure S5A-C)**. Second,
319 phosphorylation of the Pom1 substrate Rga7 was reduced in *tea1*Δ cells **(Figure S5D-E).**
320 Third, Tea4 is completely absent from the cortex of *tea1*Δ cells **(Figure S6D)**. Catalytically
321 active Pom1 autophosphorylates and requires Tea4-dependent dephosphorylation for
322 cortical enrichment. Thus, in *tea1*Δ cells, Pom1 likely binds to the membrane because it
323 cannot autophosphorylate properly. Finally, we note that Pom1 localization in *tea1*Δ
324 mimics the localization of kinase-dead *pom1-m2* mutant **(Figure S6A-B)**. Therefore, we
325 focused on the activity and regulation of Pom1 clusters in wild type cells grown in low
326 glucose.
327
328 Fission yeast cells respond to low glucose in part by depolymerizing their
329 microtubule cytoskeleton, which leads to Pom1 redistribution to the lateral cell cortex
330 where it delays mitotic entry (Kelkar and Martin, 2015). In time-lapse TIRF microscopy
331 experiments, we observed increased numbers of discreet Pom1 puncta at the lateral cell
332 cortex under low glucose conditions **(Figure 6A)**. These puncta bound to the lateral cortex
333 more frequently than under normal glucose conditions, but the average dwell time was
334 unaffected **(Figure 6B-C)**. This increased on-rate leads to accumulation of Pom1 clusters
335 at the medial cell cortex.
336
337 We next investigated how increased numbers of Pom1 puncta at the lateral cell
338 cortex affect Cdr2 nodes using TIRF microscopy. In low glucose conditions, the number
339 of Cdr2 nodes was largely unchanged, but the fluorescence intensity of individual Cdr2
340 nodes and the overall concentration of Cdr2 at the medial cortex was significantly lower

341 **(Figure 6D-F, S7A-C)**. In *pom1*Δ cells, which grow only from one tip, Cdr2 nodes form
342 normally but invade the non-growing tip. Low glucose conditions do not measurably affect
343 Cdr2 nodes in *pom1*Δ cells, so the effects that we observed are Pom1-dependent **(Figure**
344 **6D-F)**. These results indicate that Pom1 relocalization to the lateral cortex induces partial
345 disassembly of Cdr2 nodes under low glucose. To quantify how this effect scales with
346 glucose availability, we varied the concentration of media glucose over four orders of
347 magnitude. Then, we measured the concentrations of both Pom1 and Cdr2 at both the
348 cell sides and the cell tips. As glucose was reduced, Pom1 concentration decreased at
349 cell tips and increased at cell sides, consistent with redistribution **(Figure 7A,C-D)**. In
350 contrast, Cdr2 concentration increased at cell tips and decreased at cell sides **(Figure**
351 **7B-D)**. Plots of glucose availability versus Pom1 or Cdr2 concentration produced
352 sigmoidal curves with opposite orientations **(Figure 7C-D)**. Correlation analysis of Pom1
353 and Cdr2 concentrations at cell sides show they are nearly perfectly anti-correlated
354 (Pearson's r=-0.9352, p=0.0006) **(Figure 7E-F)**. We conclude that the increasing
355 frequency of Pom1 cluster binding at the lateral cell cortex leads to progressive disruption
356 of Cdr2 nodes.
357
358 **Pom1 disrupts Wee1 bursting under glucose deprivation**
359 We next examined the downstream effects of altered Pom1-Cdr2 signaling by
360 using TIRF microscopy to monitor the previously described bursts of Wee1-mNG
361 localization at Cdr2 nodes (Allard et al., 2018). In wild-type cells, both the frequency and
362 duration of Wee1 bursts increased linearly with cell size, consistent with increased
363 inhibition of Wee1 as cells grow **(Figure 8A,B)**. In low glucose, the frequency of Wee1-
364 mNG bursts still scaled with cell size as in normal glucose. However, the duration of each
365 burst was uniformly short and independent of cell size **(Figure 8A-B)**. These same burst
366 properties were seen for Wee1-mNG bursts in kinase-dead *cdr2(E177A)* mutant cells
367 grown in normal glucose **(Figure S8A-B)**. These results indicate that Cdr2 kinase activity
368 is required for retention of Wee1 at nodes, but not for the initial binding event. Further,
369 they demonstrate that low glucose phenocopies the kinase-dead mutant, consistent with
370 Pom1-dependent inhibition of Cdr2 kinase activity.
371

372 These results suggested that attenuation of Wee1 bursting dynamics in low
373 glucose might require Pom1 redistribution. We tested this idea by examining the glucose
374 dependency of Wee1 node localization in *pom1*Δ cells. In *pom1*Δ cells growing under high
375 glucose, the Wee1 burst frequency scales with cell size but Wee1 burst duration is
376 uniformly high and independent of cell size **(Figure 8A,C)**. Unlike wild type cells, which
377 suppress Wee1 bursts in low glucose, *pom1*Δ cells show a striking increase in Wee1
378 bursts under low glucose. This increase is not cause by burst duration, which was
379 independent of both cell size and glucose concentration in *pom1*Δ cells. Rather, we
380 measured increased Wee1-mNG burst frequency in low glucose *pom1*Δ cells **(Figure**
381 **8A,C)**. The reason for this increase is unknown, and suggests the existence of additional
382 glucose-regulated pathways that operate on Cdr2-Wee1 signaling.
383
384 Wee1 localization at Cdr2 nodes leads to its inhibitory phosphorylation by Cdr2
385 and the related kinase Cdr1. To test how our TIRF-based localization results connect with
386 Wee1 phosphorylation status, we analyzed phosphorylation-dependent shifts of Wee1
387 migration using western blots **(Figure 8D)**. In high glucose, Wee1 migrates as a smear
388 of phosphorylated isoforms (Allard et al., 2018; Lucena et al., 2017). The upper,
389 hyperphosphorylated forms are increased in *pom1*Δ cells but absent in *cdr2*Δ cells. This
390 hyperphosphorylated Wee1 is lost in wild-type cells grown in low glucose, consistent with
391 reduced bursts of Wee1 localization to nodes. In contrast, Wee1 appears even more
392 hyperphosphorylated in *pom1*Δ cells grown under low glucose. This result suggests that
393 Pom1 prevents phospho-inactivation of Wee1 in response to low glucose. These
394 combined experiments support a model where Pom1 redistribution to the lateral cell
395 cortex inactivates Cdr2 nodes to relieve inhibition of Wee1 under low glucose conditions.
396

397 # Discussion:

398 In this study, we have shown that the Pom1 concentration gradient is generated
399 by oligomeric Pom1 puncta that rapidly bind and release from the plasma membrane.
400 These puncta bind more frequently at cell tips versus cell sides in high glucose media,
401 while their binding rate is increased at cell sides in low glucose media. At the medial cell
402 cortex, these puncta overlap with their inhibitory target Cdr2, which localizes in static

403 oligomeric nodes. More Cdr2 nodes are free from Pom1 inhibition as cells grow larger
404 due to different density scaling of these two structures at the medial cell cortex. Our TIRF-
405 based colocalization experiments on these structures were limited to short periods of time
406 to avoid photobleaching, partly caused by the imaging conditions needed to observe
407 these highly dynamic Pom1 clusters. Nevertheless, even over these short timescales of
408 observation, the stochastic positioning of Pom1 puncta resulted in spatiotemporal
409 colocalization with Cdr2 nodes. Given the high frequency of Pom1 puncta binding, we
410 expect that many more colocalization events occur between Cdr2 nodes and Pom1
411 clusters during the course of a full cell cycle, with the potential for Pom1 clusters to visit
412 each Cdr2 node multiple times. Thus, these rapid dynamics of Pom1 puncta interacting
413 with Cdr2 nodes must be integrated in time throughout the cell cycle, leading to the G2/M
414 transition. It appears likely that the most critical temporal window for Pom1-Cdr2
415 interactions occurs during early in G2, as *pom1*Δ show defects in Cdr2-Wee1 signaling
416 specifically in small cells (Allard et al., 2018). It will be interesting to determine how these
417 rapid interactions in small cells are integrated into the mitotic entry decision, which occurs
418 later in the cell cycle when cells are longer.
419
420 **Molecular clusters are widespread in signal transduction**
421 The Pom1-Cdr2-Wee1 signaling pathway appears to function entirely within the
422 confines of oligomeric protein clusters at the plasma membrane. The development of
423 imaging technologies with increased spatial and temporal resolution has enabled the
424 discovery of protein clustering as a paradigm in signaling. As a result, a growing number
425 of signaling events and proteins have been found in similar clustered structures that are
426 referred to as nanodomains, clusters, nanoclusters, and nodes, among other names. For
427 example, recent studies have shown how PAR-3 polarity complexes in the *C. elegans*
428 zygote form clusters to reduce random diffusion and promote vectorial transport
429 (Dickinson et al., 2017; Munro, 2017; Rodriguez et al., 2017; Wang et al., 2017). In
430 addition, major signal transduction pathways in plants are organized into protein clusters
431 on plasma membrane nanodomains (Gronnier et al., 2017). Similarly, different Ras
432 isoforms partition into distinct and exclusive clusters that digitize downstream signals in
433 animal cells (Zhou and Hancock, 2015). In immune cells, both B-cell receptors and T-cell

434 receptors form oligomeric compartments at the cell cortex (Douglass and Vale, 2005; Liu
435 et al., 2016; Maity et al., 2015). These T cell receptor clusters enrich downstream kinases
436 while excluding phosphatases (Su et al., 2016), a mechanism that could relate to
437 concentrated clusters of the kinases Pom1 and Cdr2. Clustering can have a range of
438 critical impacts on the signaling properties of these pathways, such as the clustering of
439 bacterial chemotactic receptors to generate signal amplification (Bray et al., 1998; Duke
440 and Bray, 1999; Falke, 2002). Theoretical work has suggested that clustering can reduce
441 noise by generating reaction bursts (Kalay et al., 2012), which have the capacity to
442 overcome inhibitory thresholds, such as those imparted by phosphatases, more
443 effectively than a system driven by gradual accumulation of signal. Insight into the
444 functional role of clustering for Pom1-Cdr2-Wee1 will require additional *in vivo* analysis
445 combined with *in vitro* reconstitution. We have shown that Pom1 clusters remain stable
446 through biochemical enrichment, and isolated clusters exhibit the same membrane-
447 binding properties *in vitro* as in cells. Past work has demonstrated Cdr2 nodes also remain
448 stable through biochemical fractionation (Allard et al., 2018), providing the necessary
449 tools for future dissection of the pathway in a reconstituted system.
450
451 **A new model for cortical gradient formation**
452 Our work has shown that Pom1 clusters bind to the cell cortex with different
453 frequencies along the long axis of the cell, resulting in a concentration gradient. Past work
454 suggested single Pom1 molecules (or small oligomers) bind to the membrane at tips, and
455 then diffuse directionally away from the tip before dissociating (Hachet et al., 2011;
456 Saunders et al., 2012). Clusters were proposed to dynamically assemble and
457 disassemble at the cortex from this diffusing population (Saunders et al., 2012). Our
458 findings suggest a new model for gradient formation, which is distinct from this previous
459 model in four ways. First, we found that clusters themselves form a concentration gradient
460 that emanates from the cell tips. Second, our combined imaging and biochemical
461 approaches demonstrated that clusters are stable complexes that bind and rapidly
462 release from the membrane. Third, we did not observe extensive diffusion by complexes
463 bound to the membrane. It remains possible that smaller, diffusing Pom1 complexes or
464 single molecules were not detected by our imaging approach, but we favor a model where

465 diffusion is limited to short, non-directional movements that do not contribute to gradient
466 formation. Fourth, the key step in gradient formation is a positional system that increases
467 the on-rate for Pom1 clusters at cell tips versus the cell middle. Concentration gradients
468 are found across vast size scales in biology, so the mechanism of gradient formation by
469 Pom1 clusters may have broad implications. It is also important to note that the spatial
470 gradient of on-rates for Pom1 clusters binding to the cortex may depend on a
471 concentration gradient of specific lipids in the plasma membrane. In support of this
472 hypothesis, Pom1 binds to phosphatidylserine *in vitro* (Hachet et al., 2011), and this lipid
473 is enriched at the tips of growing fission yeast cells (Haupt and Minc, 2017). Thus, further
474 investigation of these lipids and their localization dynamics could reveal additional layers
475 of this morphogen gradient.
476
477 We found that the polarity landmarks Tea1 and Tea4 provide the positional
478 information for Pom1 clusters to form a concentration gradient. Past work has shown that
479 Pom1 localizes homogenously throughout the cortex in *tea1*Δ, and does not localize to
480 the cortex in *tea4*Δ (Bähler and Pringle, 1998; Hachet et al., 2011). Based on these and
481 other results, Tea1 was proposed to recruit Tea4 to cell tips, where it promotes cortical
482 loading of Pom1 molecules. Several results suggest that additional mechanisms may
483 contribute to gradient formation. For example, we found that Pom1 clusters still bind to
484 the cortex in *tea4*Δ cells but for very short durations. Past work has also shown that Tea1
485 and Tea4 form cortical clusters that co-localize at cell tips, but these Tea1-Tea4 clusters
486 do not co-localize with Pom1 clusters (Dodgson et al., 2013). Thus, Tea1-Tea4 may
487 position binding of Pom1 clusters to the cortex through an additional mechanism. For
488 example, Tea1 and Tea4 have been shown to assemble sterol-enriched lipid domains at
489 cell tips when cells initiate polarization following exit from starvation (Makushok et al.,
490 2016). Sterols and phosphatidylserine are thought to form a common membrane domain
491 in fission yeast, suggesting that these proteins could act through the recruitment and
492 organization of lipids to generate cortical domains permissive for Pom1 cluster binding
493 (Haupt and Minc, 2017; Makushok et al., 2016).
494
495

496 **Adjustable Pom1 gradients regulate mitotic entry**

497 We propose an integrated mechanism for fission yeast cell size sensing in which
498 Cdr2 acts as an important sensor of cell size that is dynamically antagonized by cortical
499 Pom1 **(Figure 9)**. Pom1 puncta bind to the medial cell cortex in a manner that can overlap
500 with Cdr2 nodes. These dynamic Pom1 puncta and stable Cdr2 cortical nodes suggest a
501 system that monitors surface expansion, consistent with the notion that fission yeast cells
502 monitor surface area as the primary determinant of size at division (Facchetti et al., 2019;
503 Pan et al., 2014). As cells grow, the density of Pom1 clusters in the cell middle decreases
504 slightly due to their binding preference at cell tips. In contrast, the density of Cdr2 nodes
505 doubles to overcome this inhibitory Pom1 threshold. The density of Pom1 clusters and
506 the resulting inhibitory threshold can be modulated by glucose availability, consistent with
507 past work (Kelkar and Martin, 2015). As fission yeast cells begin to starve due to depletion
508 of nutrients such as glucose, their length at division progressively decreases and the
509 length of the cell cycle increases (Pluskal et al., 2011; Yanagida Mitsuhiro et al., 2011).
510 The Pom-Cdr2 network has a very prominent role in this nutrient modulation, suggesting
511 that it may represent a key physiological role for the pathway (Kelkar and Martin, 2015).
512 We found that the size dependence of Wee1 localization bursts to Cdr2 nodes, which
513 facilitate Wee1 inhibition, was dampened in low glucose conditions. Re-localization of
514 Pom1 clusters to the medial cortex likely mediates this response. However, for *pom1*Δ
515 mutants in low glucose, Wee1 localization to nodes exceeds even wild type cells in high
516 glucose. This result indicates that additional mechanisms contribute to Wee1 regulation
517 in low glucose, for example Wee1 nuclear transport could be altered under these
518 conditions.

519

520 **The Pom1 gradient as a read-out for cell polarity**

521 More broadly, our study reveals the adjustable nature of the concentration gradient
522 formed by Pom1 clusters. Concentration of Pom1 clusters at cell tips reads out the polarity
523 state of the cell for downstream signaling by Cdr2 and Wee1. Conditions that alter the
524 polarized growth state of the cell would lead to changes in the gradient of Pom1 clusters,
525 resulting in altered cell size at division. This dynamic system appears to operate in a
526 manner that depends on both cell size and nutrient availability. Identification of additional

527 growth and environmental conditions that alter the relative distributions of Pom1 clusters
528 and Cdr2 nodes, and determination of how they connect with other cell cycle signaling
529 pathways, may reveal new mechanisms for nutrient modulation of cell size control.
530
531 **Integration of the Pom1-Cdr2-Wee1 pathway with other sizing mechanisms**
532 Pom1-Cdr2-Wee1 signaling is cell size dependent but is not the only pathway that
533 contributes to the overall cell size control network. Intriguingly, a recent study reported
534 that *cdr*2Δ cells no longer divide based on accumulation of a threshold surface area and
535 instead revert to a secondary mechanism of cell size control based on volume sensing.
536 These results demonstrate that cells use different signal transduction networks to
537 measure different aspects of their size. Whereas the Pom1-Cdr2 network is well suited to
538 measure cortical surface area, size-control systems that measure other aspects of size
539 would require different signaling logic. Theoretically, mechanisms for cell volume sensing
540 could depend on proteins whose concentrations do not scale linearly with cell size. Such
541 mechanisms are thought to underlie cell size control in other organisms, such as the
542 budding yeast, where growth-dependent dilution of the transcriptional repressor Whi5 is
543 thought to underlie G_1/S size control (Schmoller et al., 2015). One possible candidate for
544 cellular volume sensing in fission yeast is Cdc25, which increases in concentration with
545 cell size (Keifenheim et al., 2017; Moreno et al., 1990). These mechanisms are attractive
546 candidates for volume sensors because cytoplasmic concentration is independent of cell
547 geometry. The existence of sizing mechanisms that measure other aspects of cell size,
548 and function independently of the Pom1-Cdr2 surface area sensing network, underscores
549 that cell size is a systems level property controlled by multiple signaling pathways. Thus,
550 it remains important to discover size-dependent signaling mechanisms within each
551 individual pathway, as a step towards understanding the integration of multiple pathways
552 into a larger size control system.
553
554
555
556
557

558 # Materials and Methods:

559 **Strain Construction and Media**

560 Standard *S. pombe* media and methods were used (Moreno et al., 1991). Strains
561 used in this study are listed in Supplementary Table S1. Gene tagging and deletion were
562 performed using PCR and homologous recombination (Bähler et al., 1998). The
563 mNeonGreen (mNG) sequence was used under license from Allele Biotechnology.
564

565 **TIRF Microscopy and Analysis**

566 Pom1 puncta and node components were imaged using simultaneous dual-color
567 total internal reflection fluorescence microscopy to limit excitation of fluorophores to those
568 nearest to coverslip. Imaging was performed on a commercially available TIRF
569 microscope (Micro Video Instruments) composed of a Nikon Eclipse Ti microscope base
570 equipped with a 100x Nikon Apo TIRF NA 1.49 objective and a two-camera imaging
571 adaptor (Tu-CAM, Andor Technlogy) containing a dichroic and polarization filters
572 (Semrock FF580-FDi01-25x36, FF02-525/40-25, FF01-640/40-25) to split red and green
573 signal between two aligned Andor iXon electron-multiplied CCD cameras (Andor
574 Technology). Red/green beam alignment was performed prior to imaging using a
575 TetraSpeck Fluorescent Microsphere size kit (Thermofisher).
576

577 Standard #1.5 glass coverslips were RCA cleaned before use to remove
578 fluorescent debris. Cells were grown in EMM4S, and washed into fresh EMM4S
579 immediately before imaging to remove auto-fluorescent debris resulting from overnight
580 culture. Cells were imaged in EMM4S media on glass slides at ambient temperature.
581 Individual slides were used for no more than five minutes to prevent cells from exhausting
582 nutrients or oxygen. Agar pads were not used due to increased background fluorescence.
583

584 Image analysis and processing was performed using ImageJ2 (NIH). Cdr2 node
585 numbers and Pom1/Wee1 puncta number, frequency and binding duration were
586 quantified using the Trackmate plugin (Tinevez et al., 2017). Due to variable fluorescence
587 intensity in different TIRF fields and images, thresholding parameters were determined
588 separately for each image, and accuracy was confirmed by visual inspection to ensure

589 that only nodes/puncta were counted and that no nodes/puncta were omitted. For Wee1
590 burst and Pom1 puncta tracking, Particle Diameter was set to 0.3 microns (approximate
591 lateral resolution), with Maximum Gap Linking set to 2 frames, and Linking Range for
592 particle tracking was set to 0.15 microns. Lookup table was adjusted to fire for some
593 images to emphasize signal intensities.
594
595 **"Head-On" Tip Imaging**
596 "Head-On' or "Tip" imaging was performed using a protocol modified from
597 (Dodgson et al., 2013). Custom micro-well coverslips or Ibidi Sticky-Slide VI channels
598 (Ibidi, Martinsried, Germany) were coated with BS-I lectin (1mg/mL in water) by incubation
599 for 30 minutes and washed 3X with water to remove non-adherent lectin. Cells were then
600 added to the imaging chambers and allowed to settle to the cover-slip bottom where they
601 adhere to the lectin. Cells oriented with the long axis perpendicular to the coverslip were
602 identified using brightfield prior to fluorescence imaging.
603
604 **Spinning Disc Microscopy and Analysis**
605 Spinning-disc confocal imaging was performed using a commercially available
606 system (Micro Video Instruments, Avon, MA) featuring a Nikon Eclipse Ti base equipped
607 with an Andor CSU-W1 two-camera spinning disc module, dual Zyla sCMOS cameras
608 (Andor, South Windsor, CT) an Andor ILE laser module, and a Nikon 100X Plan Apo λ
609 1.45 oil immersion objective. Cells were imaged in EMM4S media on glass slides at
610 ambient temperature unless otherwise noted.
611
612 **Airyscan Super-Resolution Microscopy and Analysis**
613 To achieve maximum resolution and sensitivity, fluorescence intensity of Pom1
614 puncta on both cell sides and cell tips was measured using a Zeiss Airyscan microscope
615 **(Figure S1I-K)**, composed of a Zeiss LSM-880 laser scanning confocal microscope
616 (Zeiss, Oberkochen, Germany) equipped with 100X alpha Plan-Apochromat/NA 1.46 Oil
617 DIC M27 Elyra objective, Airyscan super-resolution module and GaAsP Detectors, and
618 Zen Blue acquisition software using the Super-resolution mode with pin-hole size of 1.2
619 airy-units to prioritize resolution. Z-volumes of 16 slices with 0.19μm spacing for high

620 spatial resolution in all dimensions were centered on the cell cortex closest to the
621 coverslip. Airyscan images were processed in Zeiss Zen Blue software, and quantification
622 was performed on sum projections of Airyscan reconstructed stacks.
623
624 **Pom1 and Cdr2-CTD Purification**
625 The full length Pom1 sequence, and the Cdr2-CTD fragment were purified as
626 follows: Each sequence was subcloned into pGEX6P1 vector using the Xho1 restriction
627 site and expressed as a GST-fusion protein in *Escherichia coli* strain BL21(DE3).
628 Transformants were cultured to log-phase at 37˚C, followed by a shift to 25˚C for 30
629 minutes. Expression was then induced by addition of 1-thio-β-D-galactopyranoside to
630 200μM, followed by growth for an additional 3 hours at 25˚C. Cells were harvested by
631 centrifugation and lysed by passing them twice through a French press in lysis buffer
632 (1xPBS, 100mM NaCl, 1mM DTT, and complete EDTA-free protease inhibitor tablets (1
633 tablet/50mL Buffer) (Roche, Basel, Switzerland)). Following lysis, Triton-X 100 was added
634 to 1% V/V. Lysates were then cleared by centrifugation for 10 minutes at 12,000 x g at
635 4˚C in a Sorval SS-34 fixed-angle rotor (Thermo Scientific, Waltham, MA). The
636 supernatant was then incubated with glutathione-agarose (Sigma Aldrich, St. Louis, MO)
637 for 2h at 4˚C. 20 mM glutathione (pH 8.0) was used to elute purified protein, and the
638 eluate was dialyzed overnight at 4˚C into 10mM Tris-HCl, pH8 + 5% V/V glycerol.
639
640 **Preparation of Yeast Extracts**
641 Fission yeast detergent extracts were prepared by growing 1.5L cells to mid-log
642 phase (OD ~0.3), and then washed twice with 50mL Node Isolation Buffer (NIB – 50mM
643 HEPES, 100mM KCl, 1mM $MgCl_2$, 1mM EDTA, pH 7.5) (Allard et al., 2018). Next, we
644 resuspended the pellet in an equal volume of 2X NIB (W/V) containing a
645 protease/phosphatase inhibitor cocktail (10μL/mL 200x PI, 50μL/mL 1M β-glycerol
646 phosphate, 50μL/mL 1M NaF, 2.5 μL/mL 200mM PMSF, 1mM DTT), and snap froze the
647 resuspension as pellets by pipetting drop-wise into a liquid nitrogen bath. Then, yeast
648 pellets were ground using liquid-nitrogen chilled coffee-grinders for 2 min, and collected
649 into chilled falcon tubes and stored at -80˚C. 1.5g of frozen yeast powder was then thawed
650 on ice, and Triton X-100 was added to a final concentration of 1%, and the extracts were

651 mixed by gentle pipetting. Extracts were then centrifuged at 4˚C for 10min at 20,000 x g
652 to yield a low speed supernatant, which were then used for subsequent experiments.
653
654 **Sucrose Gradient Ultracentrifugation**
655 Discontinuous sucrose gradients were prepared in 14 x 89mm Ultra Clear
656 Ultracentrifuge tubes (Beckman Coulter, Brea, CA) by layering 5 – 23% (top to bottom)
657 sucrose in NIB + 1% Triton X-100 in 0.37mL steps of 2% sucrose increments. 700µL of
658 yeast extract or recombinant protein diluted in NIB Buffer was then added to the top of
659 the gradient. Sucrose gradients were centrifuged at 100k x g (50kRPM) in a Beckman L8-
660 M ultracentrifuge for 2hr at 4˚C in a chilled SW60ti swinging bucket rotor. 0.5mL gradient
661 fractions were collected from the top by hand, vortexed, and 100µL of each fraction was
662 mixed 2:1 in 3X SDS-PAGE sample buffer (65 mM Tris pH 6.8, 3% SDS, 10% glycerol,
663 10% 2-mercaptoethanol, 50 mM NaF, 50 mM β-glycerophosphate, 1 mM sodium
664 orthovanadate) and boiled for 5 min. Samples were then subjected to SDS-PAGE and
665 western blotting or Coomassie staining. To calculate S-values of sedimentation peaks
666 from western blot signal intensities, mean band intensities were measured using Image
667 Studio Lite (LICOR, Lincoln, NE), and Gaussian Curves were fit to these values. The peak
668 of the Gaussian for each sedimentation peak of each protein was used to assign the
669 known or interpolated S-value.
670
671 **Western Blotting**
672 For western blots, cells were lysed in 150 µl of 3X SDS-PAGE sample buffer with
673 glass beads in a Mini-beadbeater-16 (Biospec, Bartlesville, OK) for 2 minutes. Gels were
674 run at a constant 20 mAmps until 75kDa marker was at the bottom of the gel. Blots were
675 probed with anti-HA (Covance, Princeton, NJ) or homemade anti-GST. For monitoring
676 Wee1 phosphorylation, samples were run on an SDS-PAGE gel containing 6%
677 acrylamide and 0.02% bisacrylamide, and then probed with a homemade anti-Wee1
678 antibody (Allard et al., 2018).
679
680 **Supported Lipid Bilayers**

681 To prepare supported lipid bilayers, we first prepared small unilamellar vesicles
682 (SUVs) composed of three lipids: (1) DOPC (18:1 (Delta9) Cis PC - 1,2 Dioleoyl-sn-
683 glycero-3-phosphocholine), (2) DOPS (18:1 PS - 1,2-Dioleoyl-sn-Glycero-3-[Phospho-L-
684 Serine]), and (3) fluorescent 18:1 Liss Rhod PE (1,2-dioleoyl-sn-glycero-3-
685 phosphoethanolamine-N-(lissamine rhodamine B sulfonyl). All lipids were dissolved in
686 chloroform (Avanti, Alabaster, AL). 2μmol total lipid with the desired molar ratios were
687 mixed in glass vials with PTFE coated caps, which had been RCA cleaned and rinsed
688 three times with chloroform before use. Excess chloroform was evaporated in a vacuum
689 desiccator for 1 hour. Lipids were resuspended in 400μL SUV Buffer (50mM HEPES,
690 100mM KCl, 1mM EDTA, 1mM $MgCl_2$, pH7.5) for 5mM lipid mixture stocks. The lipid
691 mixtures were vortexed until cloudy, and then transferred to 1.5mL Eppendorf tubes and
692 subjected to ten freeze-thaw cycles using a liquid nitrogen bath and 32˚C hot plate, with
693 2 minutes of sonication in a sonicating water bath following each thaw cycle. Stocks were
694 stored at -80˚C in 20μL aliquots.
695
696 Supported lipid bilayers were made by adding 10μL of SUVs to RCA cleaned
697 custom microwells built on 22x40mm #1.5 coverslips. Chambers were then incubated at
698 37°C for one hour to induce vesicle fusion, and unincorporated vesicles were rinsed away
699 using five rinses with 100μL SUV buffer. Yeast extract was added to these chambers by
700 removing 90μL of buffer, leaving just enough to cover the chamber bottom, and then
701 adding extract.
702
703 **Pom1 Immunoprecipitation**
704 Cultures were grown in EMM4S media to log phase, and a volume equivalent to
705 200 optical density units were harvested by centrifugation. The pellet was washed in
706 Wash Buffer (1X PBS, 250mM NaCl, 1mM EDTA, 1mM PMSF, 50mM NaF, 50mM β-
707 glycerophosphate, 1mM sodium orthovanadate, and 1% Triton X-100, and complete
708 EDTA-free protease inhibitor cocktail (1 tablet/50mL) (Roche)). The pellet was then
709 resuspended in 5mL of wash buffer, and divided into 1.5mL screw-cap tubes each with
710 200μL glass beads for lysis by bead-beading for 2 minutes using a mini-Beadbeater-16
711 (Biospec) at 4˚C. Lysates were cleared by centrifugation at 16,000 x g for 10 minutes at

712 4˚C in an Eppendorf 5415C centrifuge. The supernatant was then incubated with rotation
713 at 4˚C for 1 hour with Pierce anti-HA magnetic beads (Thermo Scientific). Beads were
714 washed five times for 15 minutes each in Wash Buffer prior to use. Beads were
715 resuspended in Kinase Assay Buffer (see below) for immediate use in kinase assays.
716
717 ***In vitro* kinase assays**
718 For *in vitro* kinase assays, immunoprecipitated Pom1 proteins and purified Cdr2-
719 CTD were combined at a 1:1 ratio in Kinase Assay Buffer (20mM Tris pH 8, 100mM NaCl,
720 50mM NaF, 50mM β-glycerophosphate, 1mM sodium orthovanadate, 10mM $MgCl_2$,
721 20μM ATP-γ-S) for 30 minutes at 30˚C. The reaction was halted by addition of EDTA to
722 20mM. For subsequent analysis by anti-thiophosphate western blot, proteins in *in vitro*
723 kinase assays were then alkylated by addition of p-nitrobenzyl mesylate to 2.5mM, and
724 incubation at 25˚C for one hour. Samples were then prepared for western blot as
725 described above. Thiophosphate western blots were probed with an antibody against
726 thiophosphate-ester (Abcam 92570) (Abcam, Cambridge, United Kingdom).
727
728
729
730 # Figure Legends:
731
732 Figure 1: **The Pom1 gradient is formed by time-averaging of puncta that transiently**
733 **bind the cortex with different dynamics along the long axis of the cell. (A)** Individual
734 frame (top panel) and sum projections (bottom panel) of high-speed TIRF microscopy
735 movie. Scale bar 1μm. Movie was continuous 15s time-lapse acquisition of 200ms
736 exposures. Blue arrows mark position of line scans performed for data in panel B. **(B)**
737 Line scans of fluorescence intensity along the long axis of the snap shot and projection
738 images in panel (A). Note that time-averaging of Pom1 puncta smoothens the
739 concentration gradient. **(C)** Traces of single-particle diffusion paths generated from a 15s
740 time-lapse TIRF microscopy acquisition of Pom1-mNeonGreen. Scale bar 1μm. **(D-E)**
741 Pom1-mNeonGreen forms puncta both at the cell tip and cell side. Images are sum
742 projections of three consecutive 200ms exposures from continuous time-lapse TIRF

743 microscopy acquisitions of either the cell tip or side as depicted in the cartoon diagrams.
744 Scale bar 1μm. **(F-H)** Particle-tracking analysis of 2μm x 2μm ROIs from 30s continuous
745 time-lapse TIRF acquisitions of Pom1-mNeonGreen at either the cell tip or side was used
746 to measure and compare (F) the binding frequency of Pom1 puncta (****, p=<0.0001),
747 (G) the average displacement of individual puncta (***, p=0.0002), (H) the binding
748 duration of individual puncta (n.s., p=0.6747). Each data point represents a single cell
749 mean, and line and error bars represent mean and standard deviation of all cells.
750 Statistical significance was tested using a Student's T-test. **(I)** Histogram of the
751 fluorescence intensity of individual Pom1 puncta at the cell tip and cell side. Puncta were
752 binned by fluorescence intensity and displayed as a population frequency.
753
754 Figure 2: **Pom1 puncta are stable structures that can be isolated *in vitro.* (A)** TIRF
755 microscopy image reveals fluorescent puncta in the extruded cytoplasm (white dotted
756 line) from a lysed Pom1-mNeonGreen cell (yellow dotted line). Scale bar 5μm. **(B)** TIRF
757 microscopy images of cell extracts prepared from wild-type (no tag) or Pom1-
758 mNeonGreen cells. Images are 50 frame sum projections of continuous 200ms time-lapse
759 exposures. The two images were contrasted equally. Scale bar 1μm. **(C)** Cytoplasmic
760 extracts of *pom1-3HA* cells were subjected to velocity sucrose gradient sedimentation,
761 and fractions were probed against the HA tag (upper blot). Fraction 1 corresponds to the
762 top of the gradient and contains smaller structures; fraction 12 corresponds to bottom of
763 the gradient and contains larger structures. Fractions 6-8 were pooled, sucrose was
764 removed by dialysis, and then the sample was subjected to a second identical round of
765 sucrose gradient sedimentation and western blotting of the resulting fractions (lower blot).
766 **(D)** Quantification of Pom1-3HA band intensities from western blot of yeast extracts in
767 panel C. Each apparent peak was fit to a gaussian curve, and S-values were determined
768 using size-standards run on identical gradients. **(E)** TIRF microscopy of Pom1-mNG
769 puncta from cytoplasmic extracts on supported lipid bilayers. Scale bar 1μm. Left panel
770 is single time point image. Right panel is kymograph taken from line scan of time-lapse
771 TIRF experiment. **(F)** Quantification of binding duration of Pom1-mNG puncta on
772 supported lipid bilayers by TIRF microscopy as in panel F. Values are compared to
773 cellular measurements of pooled tip and side localized Pom1 puncta (n.s., p=0.0514). **(G)**

774 Purified GST-Pom1 was subjected to sucrose gradient sedimentation and the fractions
775 were probed against the GST tag (upper blot). Purified GST-Pom1 was also added into
776 wild-type cell or *pom1*Δ cell extracts and incubated for 1hr at 4˚C in the presence of ATP
777 before velocity sucrose sedimentation and western blotting (bottom blots).
778
779 Figure 3: **Polarity landmarks pattern cortical dynamics of Pom1 puncta to shape the**
780 **gradient. (A)** Western blots of sucrose gradient fractions after sedimentation analysis as
781 in Figure 1C of extracts prepared from *tea1*Δ or *tea4*Δ cells expressing Pom1-3HA. **(B)**
782 Confocal micrographs of Pom1-mNG in *tea1*Δ or *tea4*Δ cells. Images are from the middle
783 focal plane; scale bar 5µm. **(C)** TIRF micrographs of Pom1-mNG localization at the tip or
784 side cortex in *tea1*Δ or *tea4*Δ cells. Scale bar 1µm. **(D)** The mean binding frequency of
785 Pom1-mNG puncta at the tips and sides of wild-type, *tea1*Δ or *tea4*Δ cells, measured by
786 TIRF microscopy. **(E)** The mean binding duration of Pom1-mNG puncta at the tips and
787 sides of wild-type, *tea1*Δ or *tea4*Δ cells, measured by TIRF microscopy. For D-E, wild-
788 type data are replotted from Figure 1. Each data point represents a single cell mean, and
789 line and error bars represent mean and standard deviation of all cells. Comparisons are
790 1-way ANOVA with Tukey's multiple comparisons tests. **** indicates $p < 0.0001$, n.s.
791 indicates $p > 0.05$.
792
793 Figure 4: **Scaling of Pom1 puncta and Cdr2 nodes at the lateral cell cortex. (A)** A
794 subset of Pom1 puncta colocalize with Cdr2 nodes. Images are dual-channel
795 simultaneously-acquired TIRF microscopy images of cells expressing Pom1-mNG and
796 Cdr2-tagRFP-t. Yellow dashed brackets outline the ROI of the lower zoomed panels.
797 Orange arrows point to Pom1 puncta colocalized with Cdr2 nodes. Scale bar is 1µm**. (B)**
798 Kymographs generated using the ROI drawn on the merged zoom image in panel A. Cyan
799 arrows indicate prominent Pom1 puncta, magenta arrows indicate prominent Cdr2 nodes,
800 and orange arrows adjacent to the merged kymograph indicate colocalization. **(C)**
801 Localization of Cdr2-mEGFP (upper panels) or Pom1-mNG (lower panels) in
802 representative cells of increasing size by TIRF microscopy. Scale bar is 1µm. **(D)** Total
803 number of Cdr2-mEGFP nodes (blue circles) or Pom1-mNG puncta (red squares)
804 measured per cell by TIRF microscopy. Quantification is limited to puncta detected and

805 resolvable in the TIRF illumination field. The slopes of the corresponding linear
806 regressions are not significantly different (*p*=0.3757). **(E)** Density of Cdr2-mEGFP nodes
807 (blue circles) or Pom1-mNG puncta (red squares) in 2x2μm square ROIs at the cell middle
808 using TIRF microscopy. **(F)** Example of colocalization analysis for Pom1 puncta and Cdr2
809 nodes. The spot detection algorithm in TrackMate plugin for ImageJ2 was used to assign
810 0.3 μm diameter circular ROIs to Cdr2 nodes (cyan) and Pom1 puncta (magenta) in
811 images such as panel A. Structures were counted as colocalized if the ROI assigned to
812 one channel overlapped with the middle of the ROI of the other channel (right panel,
813 yellow circles). Adjacent structures that failed this criterion were deemed not to be
814 colocalized (right panel, grey circles). **(G)** Ratio of free Cdr2 nodes to free Pom1 puncta,
815 plotted as a function of cell size.
816
817 Figure 5: **Properties of Pom1 puncta in *tea1*Δ cells. (A)** Localization of Pom1-mNG in
818 wild-type or *tea1*Δ cells imaged by confocal microscopy at focal planes in the cell middle.
819 Scale bar, 5μm. **(B)** Comparison of Pom1 concentration along 2μm cortical line scans
820 positioned at the cell middle of wild-type and *tea1*Δ cells, from images as in panel A.
821 Significance was tested using a Student's T-test (****, p<0.0001). **(C)** Localization of
822 Cdr2-mNG in *tea1*Δ cells by TIRF microscopy. Scale bar is 5μm. **(D)** Number of Cdr2-
823 mNG nodes as a function of cell length in wild-type (blue circles) or *tea1*Δ cells (red
824 squares), measured using TIRF microscopy images as in panel C and Figure 5A. The
825 slopes of the linear regression of each data set do not differ significantly from each other
826 (*p*=0.2029). **(E)** Localization of Wee1-mNG in *tea1*Δ cells by TIRF microscopy. Scale bar
827 is 5μm. **(F)** Number of Wee1-mNG bursts as a function of cell length in wild-type (blue
828 circles) or *tea1*Δ cells (red squares), measured using TIRF microscopy images as in panel
829 E and Figure 7A. There is a small but significant difference in the slopes of the linear
830 regressions (*p*=0.0158) such that the number of Wee1-mNG bursts scales more slowly
831 in *tea1*Δ cells than in WT. This discrepancy may result because *tea1*Δ cells can be bent
832 or T-shaped, rendering length an imperfect proxy for size.
833
834 Figure 6: **Redistribution of Pom1 puncta to the lateral cortex disrupts Cdr2 nodes**
835 **during glucose restriction. (A)** Localization of Pom1-mNG in wild-type cells grown in

836 either high (2%) or low (0.03%) glucose media. Images were collected using TIRF
837 microscopy. Scale bar, 5μm. **(B)** Comparison of the binding frequency of Pom1 puncta at
838 the lateral cell cortex in cells grown under high and low glucose measured using TIRF
839 microscopy (***, *p*=0.0003). Statistical significance was tested using a Student's T-test.
840 **(C)** Comparison of the binding duration of Pom1 puncta at the lateral cell cortex in cells
841 grown under high and low glucose measured using TIRF microscopy (n.s., *p*=0.6833).
842 Statistical significance was tested using a Student's T-test. **(D)** Localization of Cdr2-mNG
843 in wild-type or *pom1*Δ cells grown in either normal (2%) or low (0.03%) glucose media.
844 Images were collected using TIRF microscopy. Scale bar, 1μm. **(E)** Comparison of the
845 fluorescence intensity of individual Cdr2-mNG nodes in wild-type or *pom1*Δ cells grown
846 in either normal (2%) or low (0.03%) glucose media. Cdr2 nodes in wild-type cells become
847 significantly smaller under low glucose conditions (****, *p*<0.0001), but there is no
848 significant difference in Cdr2 nodes size in *pom1*Δ cells grown in normal vs low glucose
849 (n.s., *p*=0.4015). Measurements were taken from Airyscan Super-Resolution confocal
850 micrographs. **(F)** Quantification and comparison of the total number of Cdr2-mNG nodes
851 visible in TIRF micrographs of wild-type or *pom1*Δ cells grown in either normal (2%) or
852 low (0.03%) glucose media. There is no significant difference in any condition (*p*>0.05).
853 Statistical significance was tested using a one-way ANOVA.
854
855
856 Figure 7: **Pom1 and Cdr2 concentrations at the lateral cell cortex are anti-correlated.**
857 **(A)** Localization of Pom1-mNG in confocal micrographs at middle cell focal planes.
858 Regions where line-scans were used to measure fluorescence intensity are marked at
859 the tip and side (orange lines). Scale bar, 1μm. **(B)** Localization of Cdr2-mNG in confocal
860 micrographs at middle cell focal planes. Scale bar, 1μm. Regions where line-scans were
861 used to measure fluorescence intensity are marked at the tip and side (orange lines). **(C)**
862 Concentration of Pom1 (red squares) or Cdr2 (blue circles) at cell sides in a range of
863 glucose concentrations, measured using 'Side ROI' denoted in panels A and B. **(D)**
864 Concentration of Pom1 (red squares) or Cdr2 (blue circles) at cell tips in a range of
865 glucose concentrations, measured using 'Tip ROI' denoted in panels A and B. **(E)**
866 Correlation of Cdr2 vs Pom1 concentrations at cell sides in each glucose concentration

867 from panel C. Concentrations are anticorrelated across all tested media glucose
868 concentrations (p=0.0006, Pearson r=-0.9352). **(F)** Correlation of Cdr2 vs Pom1
869 concentrations at cell tips in each glucose concentration from panel D. Concentrations
870 show weak anticorrelation across the tested media glucose concentrations, but the
871 correlation is not statistically significant (p=0.09, Pearson r=-0.65).
872
873 Figure 8: **Pom1 redistribution under glucose restriction disrupts Wee1 regulation at**
874 **cortical nodes. (A)** Localization of Wee1-mNG in wild-type or *pom1*Δ cells grown in
875 either high (2%) or low (0.03%) glucose media. Images were collected using TIRF
876 microscopy. Scale bar, 5μm. **(B)** Quantification of Wee1 bursting kinetics in wild-type cells
877 grown under high (2%, blue circles) and low (0.03%, red squares) glucose conditions.
878 The top panel is a plot of the total number of Wee1 bursts as a function of cell length,
879 counted in single time point TIRF micrographs. The slopes of the linear regressions are
880 significantly different (p<0.0001, $R^2_{2\%}$=0.66, $R^2_{0.03\%}$=0.45). The middle panel is a plot of
881 the frequency of Wee1 bursts as a function of cell length, measured using the TrackMate
882 particle tracking algorithm on TIRF microscopy movies. The slopes of the linear
883 regressions are not significantly different (p=0.8426, $R^2_{2\%}$=0.50, $R^2_{0.03\%}$=0.51). The
884 bottom panel is a plot of Wee1 burst duration as a function of cell length, measured using
885 the TrackMate particle tracking algorithm on TIRF microscopy movies. The slopes of the
886 linear regressions are not significantly different (p=0.09, $R^2_{2\%}$=0.28, $R^2_{0.03\%}$=0.05), but the
887 values of the elevation of the regressions are significantly different (p=0.0005). **(C)**
888 Quantification of Wee1 bursting kinetics in *pom1*Δ cells grown under normal (2%, green
889 circles) and low (0.03%, magenta squares) glucose conditions. The top panel is a plot of
890 the total number of Wee1 bursts as a function of cell length, counted in single time point
891 TIRF micrographs. The slopes of the linear regressions are not significantly different
892 (p=0.09, $R^2_{2\%}$=0.45, $R^2_{0.03\%}$=0.54), but the values of the elevation of the regressions are
893 significantly different (p<0.0001). The middle panel is a plot of the frequency of Wee1
894 bursts as a function of cell length, measured using the TrackMate particle tracking
895 algorithm on TIRF microscopy movies. The slopes of the linear regressions are not
896 significantly different (p=0.3125, $R^2_{2\%}$=0.45, $R^2_{0.03\%}$=0.56) but the values of the elevation
897 of the regressions are significantly different (p=0.009). The bottom panel is a plot of Wee1

898 burst duration as a function of cell length, measured using the TrackMate particle tracking
899 algorithm on TIRF microscopy movies. The slopes of the linear regressions are not
900 significantly different (p=0.8352, $R^2_{2\%}$=0.3, $R^2_{0.03\%}$=0.002), and the values of the
901 intercepts of the regressions are not significantly different (p=0.5392). For (B-C), b_1
902 denotes slope and b_0 denotes the Y-intercept. **(D)** Western blot of Wee1 in wild-type,
903 *pom1*Δ, and *cdr2*Δ cells grown in high (2%) or low (0.03%) glucose media showing
904 phosphorylation dependent band-shifts. Whole cell extracts were separated by SDS-
905 PAGE, and blots were probed with an α-Wee1 antibody.
906
907
908 Figure 9: **A model for the glucose-modulated control of Wee1 bursting by Pom1 and**
909 **Cdr2.** See text for discussion.
910
911 Supplemental Figure S1 (Figure 1): **Analysis of the Pom1 gradient by confocal**
912 **microscopy**. **(A)** Similar to TIRF microscopy, at middle-cell focal planes, discreet Pom1-
913 mNeonGreen puncta are apparent at the lateral cell cortex of cells in individual frames
914 (200ms) of spinning-disc microscopy movies. Scale bar 1μm. **(B)** Individual Pom1 puncta
915 become averaged out in a projection of the entire continuous spinning-disc confocal
916 microscopy movie. Sum projection of a continuous 15s time-lapse acquisition of 200ms
917 exposures. **(C)** A line scan along the cell-perimeter in the direction indicated by the arrow
918 of the single time-point micrograph of the cell in (A) reveals that Pom1 puncta form a noisy
919 concentration gradient that begins at the cell tip and decays toward the cell middle. **(D)**
920 The same line scan as in panel C, but of the time-lapse sum projection of the cell in panel
921 B. This plot demonstrates that time-averaging of Pom1 puncta smoothens the
922 concentration gradient. **(E)** Spinning-disc confocal micrographs of single 200ms
923 acquisitions and **(F)** sum-projections of time lapse movies as in panels A and B
924 respectively, but using a top-focal plane. **(G-H)** Line scan using a straight line across the
925 long axis of the cell indicated by the arrow head on both the single time-point (G) and sum
926 projection (H) of a 15s continuous time-lapse movie. **(I-J)** Representative images of
927 Airyscan super-resolution micrographs of Pom1-mNeonGreen at either the cell tips (I) or
928 cell side (J). Images are sum projections of sequential five-frame Z-stacks spaced 0.17μm

929 apart, positioned to include all detected cortical Pom1-mNeonGreen signal. Scale bar,
930 1µm. **(K)** Fluorescence intensities of all single puncta resolved in Airyscan images as in
931 panels I-J. Data points represent individual puncta values, error bars are the mean and
932 standard deviation.
933
934 Supplemental Figure S2 (Figure 2): **Controls and supporting *in vitro* analysis of Pom1**
935 **puncta. (A)** Fluorescence intensity trace of a single Pom1 puncta binding to the cell
936 cortex, measured by high speed TIRF microscopy of a cell expressing Pom1-mNG (~50
937 frames per second with continuous acquisition). Rapid intensity changes indicating
938 binding and unbinding are indicated by green upward and magenta downward pointing
939 arrows respectively. **(B)** Size standards for velocity sucrose gradients, as in main Figure
940 2C-E. Data are quantified from single Coomassie-stained gels, or using
941 spectrophotometry data. **(C)** Plot of S-value versus sedimentation pattern. Line is linear
942 regression of the three size standards, with the S-value for Pom1 peaks interpolated. **(D)**
943 Quantification and comparison of binding duration of either wild-type or kinase-dead
944 Pom1-mNG to supported lipid bilayers in TIRF microscopy movies (***p=<0.0001).
945 Statistical significance was tested with a Student's T-test. **(E)** FRAP analysis of supported
946 lipid bilayers. Upper panel: A circular ROI (teal dashed line) was used to bleach
947 fluorescent PE in the bilayers. Lower panel: Kymograph at white dashed line in upper
948 panel of fluorescence recovery as monitored by TIRF microscopy, indicating fluidity.
949
950 Supplemental Figure S3 (Figure 3): **Representative single-cell data used to compute**
951 **mean cellular values in Figure 3. (A)** Quantification of binding duration of individual
952 Pom1-mNG puncta at the tips or sides of representative wild-type, *tea1*Δ or *tea4*Δ cells,
953 measured by TIRF microscopy. **(B)** Quantification of total displacement of individual
954 Pom1-mNG puncta at the tips or sides of representative wild-type, *tea1*Δ or *tea4*Δ cells,
955 measured by TIRF microscopy. For A-B, line and error represent single cell mean and
956 standard deviation.
957
958 Supplemental Figure S4 (Figure 4): **Supporting analysis of Cdr2 nodes and Pom1**
959 **puncta at the medial cell cortex. (A)** Comparison of Pom1 puncta binding frequency on

960 the cell sides of wild-type and *cdr2*Δ cells (n.s., *p*=0.1076). **(B)** Comparison of Pom1
961 puncta binding duration on the cell sides of wild-type and *cdr2*Δ cells (n.s., *p*=0.371). **(C)**
962 Comparison of Pom1 puncta displacement on the cell sides of wild-type and *cdr2*Δ cells
963 (n.s., *p*=0.8191). In A-C, significance was tested using a Student's T-test. **(D)** Schematic
964 and quantification of Pom1 concentration at the lateral cell cortex measured by confocal
965 microscopy, using 2μm line scans at the cell middle from images such as Figure 5A. The
966 slope of the linear regression is negative, but not significantly non-zero (*p*=0.2603,
967 R^2=0.03). **(E)** Plot of the number of colocalized structures counted in a middle cell 2x2μm
968 ROI as a function of cell size. The slope of the linear regression is significantly non-zero
969 (*p*=0.0006, R^2=0.3). **(F)** Plot of free, non-colocalized Cdr2 nodes (blue circles) and Pom1
970 puncta (red squares). The slope of the linear regression of #Pom1 puncta versus cell
971 length is negative, and significantly non-zero (*p*=0.001, R^2=0.27). The slope of the linear
972 regression of #Cdr2 nodes versus cell length is positive, and significantly non-zero
973 (*p*=0.021, R^2=0.15).
974
975 Supplemental Figure S5 (Figure 5): ***In vitro* analysis of Pom1 activity in *tea1*Δ cells.**
976 **(A)** Western blot of an *in vitro* thiophosphate kinase assay to test Pom1
977 autophosphorylation activity in *pom1-3HA*, *pom1-AS-3HA*, and *pom1-AS-3HA tea1*Δ
978 cells. Blots were probed with an α-thiophosphate antibody. Only analog-sensitive (AS)
979 alleles can use ATPγS to thio-phosphorylate substrates. **(B)** Comparison of western blot
980 band intensities from four replicate gels, derived from two separate experiments as in
981 panel A. Statistical significance was tested using a paired T-test between *Pom1-AS-3HA*
982 and *Pom1-AS-3HA tea1*Δ cells (*, *p*=0.02). **(C)** Western blot of an *in vitro* thiophosphate
983 kinase assay to measure phosphorylation of purified Cdr2 by Pom1 in *pom1-3HA*, *pom1-*
984 *AS-3HA*, and *pom1-AS-3HA tea1*Δ cells. Blots were probed with an anti-thiophosphate
985 antibody. Excess Pom1-3HA was used in lanes 1 and 3 to ensure absence of signal in
986 negative controls lacking the analog-sensitive mutation. Cdr2(712-775) is a fragment that
987 contains known Pom1 phosphorylation sites. **(D)** Western blot of the Pom1 substrate
988 Rga7-3HA in wild-type, *tea1*Δ, and *pom1*Δ cells. Whole-cell extracts were separated by
989 SDS-PAGE, and probed with α-HA antibodies. The upper band represents a Pom1-
990 dependent phospho-isoform. **(E)** Comparison of band intensities from four replicate gels

991 as in (D), expressed as the ratio of the grey-value of the top band/bottom band. Line and
992 error are mean and standard deviation. Statistical significance was tested using a one-
993 way ANOVA and Tukey's multiple comparisons test (WT vs *tea1*Δ, ***p=0.003, WT vs
994 *pom1*Δ, ****p<0.0001, *tea1*Δ vs *pom1*Δ, ****p<0.0001).
995
996 Supplemental Figure S6 (Figure 5): **Control of Pom1 concentration at the cell side.**
997 **(A)** Localization of Pom1-mNG in wild-type, *tea1*Δ, and *pom1-KD* (kinase-dead) cells at
998 the indicated concentration of glucose. Images are confocal micrographs taken at a
999 middle cell focal plane. Scale bar, 5μm. **(B)** Quantification of Pom1 concentration along
1000 2μm line scans as in figure S4D, measured using images as in panel A. The means of
1001 each column are significantly different from every other column (p<0.005). Statistical
1002 significance was tested using a one-way ANOVA and Tukey's multiple comparison's test.
1003 **(C)** Plot of Pom1 concentration at the cell side as a function of glucose concentration in
1004 the growth media. Data were fit to an exponential curve showing a negative sinusoidal
1005 relationship reaching half saturation at ~0.05% glucose. The concentration of Pom1-mNG
1006 at the lateral cell cortex in a *tea1*Δ mutant was fit to this curve, and is the approximate
1007 equivalent of wild-type cells grown in 0.03% Glucose. Line and error are mean and
1008 standard deviation. (D) Localization of Tea4-mNG in wild-type or *tea1*Δ cells grown in the
1009 indicated concentration of glucose for one hour. Images are confocal micrographs taken
1010 at middle cell focal planes. Arrows point to lateral puncta of Tea4-mNG. Scale bar, 5μm.
1011
1012 Supplemental Figure S7 (Figure 6): **Redistribution of Pom1 puncta to the lateral**
1013 **cortex disrupts Cdr2 nodes during glucose restriction, supporting data. (A)** Analysis
1014 of Pom1 and Cdr2 redistribution by spinning-disc confocal microscopy, as in (Kelkar and
1015 Martin, 2015). Images are confocal micrographs of cells co-expressing Pom1-tdTomato
1016 and Cdr2-mNG in high (2%) or low (0.03%) glucose media. Scale bar, 5μm. **(B)** Cortical
1017 fluorescence intensity of Cdr2 and Pom1 was measured using line scans drawn around
1018 the circumference of the representative cell marked with an arrowhead in the 2% glucose
1019 portion of panel A. **(C)** Cortical fluorescence intensity of Cdr2 and Pom1 was measured
1020 using line scans drawn around the circumference of the representative cell marked with
1021 an arrowhead in the 0.03% glucose portion of panel A.

1022

1023 Supplemental Figure S8 (Figure 8): **Re-plotting of data from Main Figure 8 for**
1024 **additional comparison. (A)** Plot of the frequency of Wee1 bursts as a function of cell
1025 length in wild-type cells grown in high (2%) glucose (blue circles) and low glucose (red
1026 squares), and kinase-dead *cdr2(E177A)* mutant cells grown in 2% glucose (green
1027 triangles). Measurements were made using the TrackMate particle tracking algorithm on
1028 TIRF microscopy movies. The slopes of the linear regressions are not significantly
1029 different (p=0.7651, $R^2_{2\%}$=0.5, $R^2_{0.03\%}$=0.51, $R^2_{Cdr2(E177A)}$=0.51) and the elevations of the
1030 regressions are also not significantly different (p=0.4397). **(B)** Plot of Wee1 burst duration
1031 as a function of cell length in wild-type cells grown in low glucose (red squares) and
1032 kinase-dead *cdr2(E177A)* mutant cells grown in 2% glucose (green triangles).
1033 Measurements were made using the Trackmate particle tracking algorithm on TIRF
1034 microscopy movies. The slopes of the linear regressions are not significantly different
1035 (p=0.8048, $R^2_{0.03\%}$=0.05, $R^2_{Cdr2(E177A)}$=0.2) and the elevations of the regressions are also
1036 not significantly different (p=0.8048).

1037

1038 Supplemental Table S1: Fission yeast strains used in this study.

1039

1040 Acknowledgements:

1041 We thank members of the Moseley lab and Erik Griffin for comments on the manuscript,
1042 as well as B. Wickner and C. Barlowe and the Norris Cotton Cancer Center Molecular
1043 Interactions & Imaging Core at Dartmouth for sharing equipment. A. Lavanway, Z.
1044 Svindrych and the Life Sciences Light Microscopy Facility for assistance with microscopy.
1045 A. Orr for assistance with ultracentrifugation. Youjun Wu for recombinant Pom1 proteins.
1046 This work was supported by grants from the American Cancer Society (RSG-15-140-01-
1047 CCG) and the NIH (R01 GM099774) to J.B.M; and an NIH Training Grant
1048 (T32GM008704) to C.A.H.A. Shared imaging resources were supported by grants from
1049 the NIH (1S10OD018046 and P20GM113132).

1050

1051

1052

1053 # References:

1054 Akamatsu, M., Berro, J., Pu, K.-M., Tebbs, I.R., and Pollard, T.D. (2014). Cytokinetic
1055 nodes in fission yeast arise from two distinct types of nodes that merge during interphase.
1056 J Cell Biol *204*, 977–988.

1057 Akamatsu, M., Lin, Y., Bewersdorf, J., and Pollard, T.D. (2017). Analysis of interphase
1058 node proteins in fission yeast by quantitative and superresolution fluorescence
1059 microscopy. Mol. Biol. Cell *28*, 3203–3214.

1060 Alberghina, L., Höfer, T., and Vanoni, M. (2009). Molecular networks and system-level
1061 properties. J. Biotechnol. *144*, 224–233.

1062 Aligue, R., Wu, L., and Russell, P. (1997). Regulation of Schizosaccharomyces pombe
1063 Wee1 Tyrosine Kinase. J. Biol. Chem. *272*, 13320–13325.

1064 Allard, C.A.H., Opalko, H.E., Liu, K.-W., Medoh, U., and Moseley, J.B. (2018). Cell size–
1065 dependent regulation of Wee1 localization by Cdr2 cortical nodes. J Cell Biol *217*, 1589–
1066 1599.

1067 Bähler, J., and Nurse, P. (2001). Fission yeast Pom1p kinase activity is cell cycle
1068 regulated and essential for cellular symmetry during growth and division. EMBO J. *20*,
1069 1064–1073.

1070 Bähler, J., and Pringle, J.R. (1998). Pom1p, a fission yeast protein kinase that provides
1071 positional information for both polarized growth and cytokinesis. Genes Dev. *12*, 1356–
1072 1370.

1073 Bähler, J., Wu, J.-Q., Longtine, M.S., Shah, N.G., Iii, A.M., Steever, A.B., Wach, A.,
1074 Philippsen, P., and Pringle, J.R. (1998). Heterologous modules for efficient and versatile
1075 PCR-based gene targeting in Schizosaccharomyces pombe. Yeast *14*, 943–951.

1076 Bhatia, P., Hachet, O., Hersch, M., Rincon, S.A., Berthelot-Grosjean, M., Dalessi, S.,
1077 Basterra, L., Bergmann, S., Paoletti, A., and Martin, S.G. (2014). Distinct levels in Pom1
1078 gradients limit Cdr2 activity and localization to time and position division. Cell Cycle
1079 Georget. Tex *13*, 538–552.

1080 Bray, D., Levin, M.D., and Morton-Firth, C.J. (1998). Receptor clustering as a cellular
1081 mechanism to control sensitivity. Nature *393*, 85–88.

1082 Breeding, C.S., Hudson, J., Balasubramanian, M.K., Hemmingsen, S.M., Young, P.G.,
1083 and Gould, K.L. (1998). The cdr2(+) gene encodes a regulator of G2/M progression and
1084 cytokinesis in Schizosaccharomyces pombe. Mol. Biol. Cell *9*, 3399–3415.

1085 Chang, F., and Martin, S.G. (2009). Shaping Fission Yeast with Microtubules. Cold Spring
1086 Harb. Perspect. Biol. *1*, a001347.

1087 Deng, L., and Moseley, J.B. (2013). Compartmentalized nodes control mitotic entry
1088 signaling in fission yeast. Mol. Biol. Cell *24*, 1872–1881.

1089 Deng, L., Baldissard, S., Kettenbach, A.N., Gerber, S.A., and Moseley, J.B. (2014).
1090 Dueling Kinases Regulate Cell Size at Division through the SAD Kinase Cdr2. Curr. Biol.
1091 *24*, 428–433.

1092 Dickinson, D.J., Schwager, F., Pintard, L., Gotta, M., and Goldstein, B. (2017). A Single-
1093 Cell Biochemistry Approach Reveals PAR Complex Dynamics during Cell Polarization.
1094 Dev. Cell *42*, 416-434.e11.

1095 Dodgson, J., Chessel, A., Yamamoto, M., Vaggi, F., Cox, S., Rosten, E., Albrecht, D.,
1096 Geymonat, M., Csikasz-Nagy, A., Sato, M., et al. (2013). Spatial segregation of polarity
1097 factors into distinct cortical clusters is required for cell polarity control. Nat. Commun. *4*,
1098 1834.

1099 Douglass, A.D., and Vale, R.D. (2005). Single-molecule microscopy reveals plasma
1100 membrane microdomains created by protein-protein networks that exclude or trap
1101 signaling molecules in T cells. Cell *121*, 937–950.

1102 Duke, T.A., and Bray, D. (1999). Heightened sensitivity of a lattice of membrane
1103 receptors. Proc. Natl. Acad. Sci. U. S. A. *96*, 10104–10108.

1104 Facchetti, G., Knapp, B., Flor-Parra, I., Chang, F., and Howard, M. (2019).
1105 Reprogramming Cdr2-Dependent Geometry-Based Cell Size Control in Fission Yeast.
1106 Curr. Biol. *29*, 350-358.e4.

1107 Falke, J.J. (2002). Cooperativity between bacterial chemotaxis receptors. Proc. Natl.
1108 Acad. Sci. U. S. A. *99*, 6530–6532.

1109 Fantes, P., and Nurse, P. (1977). Control of cell size at division in fission yeast by a
1110 growth-modulated size control over nuclear division. Exp. Cell Res. *107*, 377–386.

1111 Gautier, J., Solomon, M.J., Booher, R.N., Bazan, J.F., and Kirschner, M.W. (1991). cdc25
1112 is a specific tyrosine phosphatase that directly activates p34cdc2. Cell *67*, 197–211.

1113 Ginzberg, M.B., Kafri, R., and Kirschner, M. (2015). Cell biology. On being the right (cell)
1114 size. Science *348*, 1245075.

1115 Gould, K.L., and Nurse, P. (1989). Tyrosine phosphorylation of the fission yeast cdc2 +
1116 protein kinase regulates entry into mitosis. Nature *342*, 39.

1117 Gronnier, J., Crowet, J.-M., Habenstein, B., Nasir, M.N., Bayle, V., Hosy, E., Platre, M.P.,
1118 Gouguet, P., Raffaele, S., Martinez, D., et al. (2017). Structural basis for plant plasma
1119 membrane protein dynamics and organization into functional nanodomains. ELife *6*.

1120 Gu, Y., and Oliferenko, S. (2019). Cellular geometry scaling ensures robust division site
1121 positioning. Nat. Commun. *10*, 268.

1122 Guzmán-Vendrell, M., Rincon, S.A., Dingli, F., Loew, D., and Paoletti, A. (2015).
1123 Molecular control of the Wee1 regulatory pathway by the SAD kinase Cdr2. J. Cell Sci.
1124 *128*, 2842–2853.

1125 Hachet, O., Berthelot-Grosjean, M., Kokkoris, K., Vincenzetti, V., Moosbrugger, J., and
1126 Martin, S.G. (2011). A phosphorylation cycle shapes gradients of the DYRK family kinase
1127 Pom1 at the plasma membrane. Cell *145*, 1116–1128.

1128 Harashima, H., Dissmeyer, N., and Schnittger, A. (2013). Cell cycle control across the
1129 eukaryotic kingdom. Trends Cell Biol. *23*, 345–356.

1130 Haupt, A., and Minc, N. (2017). Gradients of phosphatidylserine contribute to plasma
1131 membrane charge localization and cell polarity in fission yeast. Mol. Biol. Cell *28*, 210–
1132 220.

1133 Hersch, M., Hachet, O., Dalessi, S., Ullal, P., Bhatia, P., Bergmann, S., and Martin, S.G.
1134 (2015). Pom1 gradient buffering through intermolecular auto-phosphorylation. Mol. Syst.
1135 Biol. *11*, 818.

1136 Jorgensen, P., and Tyers, M. (2004). How Cells Coordinate Growth and Division. Curr.
1137 Biol. *14*, R1014–R1027.

1138 Kalay, Z., Fujiwara, T.K., and Kusumi, A. (2012). Confining domains lead to reaction
1139 bursts: reaction kinetics in the plasma membrane. PloS One *7*, e32948.

1140 Kanoh, J., and Russell, P. (1998). The Protein Kinase Cdr2, Related to Nim1/Cdr1 Mitotic
1141 Inducer, Regulates the Onset of Mitosis in Fission Yeast. Mol. Biol. Cell *9*, 3321–3334.

1142 Keifenheim, D., Sun, X.-M., D'Souza, E., Ohira, M.J., Magner, M., Mayhew, M.B.,
1143 Marguerat, S., and Rhind, N. (2017). Size-Dependent Expression of the Mitotic Activator
1144 Cdc25 Suggests a Mechanism of Size Control in Fission Yeast. Curr. Biol. CB *27*, 1491-
1145 1497.e4.

1146 Kelkar, M., and Martin, S.G. (2015). PKA antagonizes CLASP-dependent microtubule
1147 stabilization to re-localize Pom1 and buffer cell size upon glucose limitation. Nat.
1148 Commun. *6*, 8445.

1149 Kettenbach, A.N., Deng, L., Wu, Y., Baldissard, S., Adamo, M.E., Gerber, S.A., and
1150 Moseley, J.B. (2015). Quantitative phosphoproteomics reveals pathways for coordination
1151 of cell growth and division by the conserved fission yeast kinase pom1. Mol. Cell.
1152 Proteomics MCP *14*, 1275–1287.

1153 Kumagai, A., and Dunphy, W.G. (1991). The cdc25 protein controls tyrosine
1154 dephosphorylation of the cdc2 protein in a cell-free system. Cell *64*, 903–914.

1155 Liu, W., Wang, H., and Xu, C. (2016). Antigen Receptor Nanoclusters: Small Units with
1156 Big Functions. Trends Immunol. *37*, 680–689.

1157 Lloyd, A.C. (2013). The Regulation of Cell Size. Cell *154*, 1194–1205.

1158 Lucena, R., Alcaide-Gavilán, M., Anastasia, S.D., and Kellogg, D.R. (2017). Wee1 and
1159 Cdc25 are controlled by conserved PP2A-dependent mechanisms in fission yeast. Cell
1160 Cycle *16*, 428–435.

1161 Maity, P.C., Blount, A., Jumaa, H., Ronneberger, O., Lillemeier, B.F., and Reth, M. (2015).
1162 B cell antigen receptors of the IgM and IgD classes are clustered in different protein
1163 islands that are altered during B cell activation. Sci. Signal. *8*, ra93.

1164 Makushok, T., Alves, P., Huisman, S.M., Kijowski, A.R., and Brunner, D. (2016). Sterol-
1165 Rich Membrane Domains Define Fission Yeast Cell Polarity. Cell *165*, 1182–1196.

1166 Martin, S.G., and Berthelot-Grosjean, M. (2009). Polar gradients of the DYRK-family
1167 kinase Pom1 couple cell length with the cell cycle. Nature *459*, 852–856.

1168 Masuda, H., Fong, C.S., Ohtsuki, C., Haraguchi, T., and Hiraoka, Y. (2011).
1169 Spatiotemporal regulations of Wee1 at the G2/M transition. Mol. Biol. Cell *22*, 555–569.

1170 Moreno, S., Hayles, J., and Nurse, P. (1989). Regulation of p34cdc2 protein kinase during
1171 mitosis. Cell *58*, 361–372.

1172 Moreno, S., Nurse, P., and Russell, P. (1990). Regulation of mitosis by cyclic
1173 accumulation of p80cdc25 mitotic inducer in fission yeast. Nature *344*, 549–552.

1174 Moreno, S., Klar, A., and Nurse, P. (1991). Molecular genetic analysis of fission yeast
1175 Schizosaccharomyces pombe. Methods Enzymol. *194*, 795–823.

1176 Morrell, J.L., Nichols, C.B., and Gould, K.L. (2004). The GIN4 family kinase, Cdr2p, acts
1177 independently of septins in fission yeast. J. Cell Sci. *117*, 5293–5302.

1178 Moseley, J.B., Mayeux, A., Paoletti, A., and Nurse, P. (2009). A spatial gradient
1179 coordinates cell size and mitotic entry in fission yeast. Nature *459*, 857–860.

1180 Munro, E. (2017). Protein Clustering Shapes Polarity Protein Gradients. Dev. Cell *42*,
1181 309–311.

1182 Neumann, F.R., and Nurse, P. (2007). Nuclear size control in fission yeast. J. Cell Biol.
1183 *179*, 593–600.

1184 Opalko, H.E., and Moseley, J.B. (2017). Dynamic regulation of Cdr1 localization and
1185 phosphorylation during osmotic stress. J. Biol. Chem. jbc.M117.793034.

1186 Pan, K.Z., Saunders, T.E., Flor-Parra, I., Howard, M., and Chang, F. (2014). Cortical
1187 regulation of cell size by a sizer cdr2p. ELife *3*.

1188 Pluskal, T., Hayashi, T., Saitoh, S., Fujisawa, A., and Yanagida, M. (2011). Specific
1189 biomarkers for stochastic division patterns and starvation-induced quiescence under
1190 limited glucose levels in fission yeast. FEBS J. *278*, 1299–1315.

1191 Rincon, S.A., Bhatia, P., Bicho, C., Guzman-Vendrell, M., Fraisier, V., Borek, W.E., Alves,
1192 F. de L., Dingli, F., Loew, D., Rappsilber, J., et al. (2014). Pom1 regulates the assembly
1193 of Cdr2–Mid1 cortical nodes for robust spatial control of cytokinesis. J Cell Biol *206*, 61–
1194 77.

1195 Rodriguez, J., Peglion, F., Martin, J., Hubatsch, L., Reich, J., Hirani, N., Gubieda, A.G.,
1196 Roffey, J., Fernandes, A.R., St Johnston, D., et al. (2017). aPKC Cycles between
1197 Functionally Distinct PAR Protein Assemblies to Drive Cell Polarity. Dev. Cell *42*, 400-
1198 415.e9.

1199 Russell, P., and Nurse, P. (1986). cdc25+ functions as an inducer in the mitotic control of
1200 fission yeast. Cell *45*, 145–153.

1201 Russell, P., and Nurse, P. (1987). Negative regulation of mitosis by wee1+, a gene
1202 encoding a protein kinase homolog. Cell *49*, 559–567.

1203 Saunders, T.E., Pan, K.Z., Angel, A., Guan, Y., Shah, J.V., Howard, M., and Chang, F.
1204 (2012). Noise reduction in the intracellular pom1p gradient by a dynamic clustering
1205 mechanism. Dev. Cell *22*, 558–572.

1206 Schmoller, K.M., Turner, J.J., Kõivomägi, M., and Skotheim, J.M. (2015). Dilution of the
1207 cell cycle inhibitor Whi5 controls budding-yeast cell size. Nature *526*, 268–272.

1208 Shiozaki, K. (2009). Nutrition-Minded Cell Cycle. Sci Signal *2*, pe74–pe74.

1209 Simanis, V., and Nurse, P. (1986). The cell cycle control gene cdc2+ of fission yeast
1210 encodes a protein kinase potentially regulated by phosphorylation. Cell *45*, 261–268.

1211 Strausfeld, U., Labbé, J.C., Fesquet, D., Cavadore, J.C., Picard, A., Sadhu, K., Russell,
1212 P., and Dorée, M. (1991). Dephosphorylation and activation of a p34cdc2/cyclin B
1213 complex in vitro by human CDC25 protein. Nature *351*, 242–245.

1214 Su, X., Ditlev, J.A., Hui, E., Xing, W., Banjade, S., Okrut, J., King, D.S., Taunton, J.,
1215 Rosen, M.K., and Vale, R.D. (2016). Phase separation of signaling molecules promotes
1216 T cell receptor signal transduction. Science *352*, 595–599.

1217 Tinevez, J.-Y., Perry, N., Schindelin, J., Hoopes, G.M., Reynolds, G.D., Laplantine, E.,
1218 Bednarek, S.Y., Shorte, S.L., and Eliceiri, K.W. (2017). TrackMate: An open and
1219 extensible platform for single-particle tracking. Methods *115*, 80–90.

1220 Wang, S.-C., Low, T.Y.F., Nishimura, Y., Gole, L., Yu, W., and Motegi, F. (2017). Cortical
1221 forces and CDC-42 control clustering of PAR proteins for Caenorhabditis elegans
1222 embryonic polarization. Nat. Cell Biol. *19*, 988–995.

1223 Wood, E., and Nurse, P. (2013). Pom1 and cell size homeostasis in fission yeast. Cell
1224 Cycle Georget. Tex *12*, 3228–3236.

1225 Wu, L., and Russell, P. (1993). Nim1 kinase promotes mitosis by inactivating Wee1
1226 tyrosine kinase. Nature *363*, 738–741.

1227 Wu, L., Shiozaki, K., Aligue, R., and Russell, P. (1996). Spatial organization of the Nim1-
1228 Wee1-Cdc2 mitotic control network in Schizosaccharomyces pombe. Mol. Biol. Cell *7*,
1229 1749–1758.

1230 Yanagida Mitsuhiro, Ikai Nobuyasu, Shimanuki Mizuki, and Sajiki Kenichi (2011). Nutrient
1231 limitations alter cell division control and chromosome segregation through growth-related
1232 kinases and phosphatases. Philos. Trans. R. Soc. B Biol. Sci. *366*, 3508–3520.

1233 Young, P.G., and Fantes, P.A. (1987). Schizosaccharomyces pombe mutants affected in
1234 their division response to starvation. J. Cell Sci. *88*, 295–304.

1235 Zhou, Y., and Hancock, J.F. (2015). Ras nanoclusters: Versatile lipid-based signaling
1236 platforms. Biochim. Biophys. Acta *1853*, 841–849.

1237

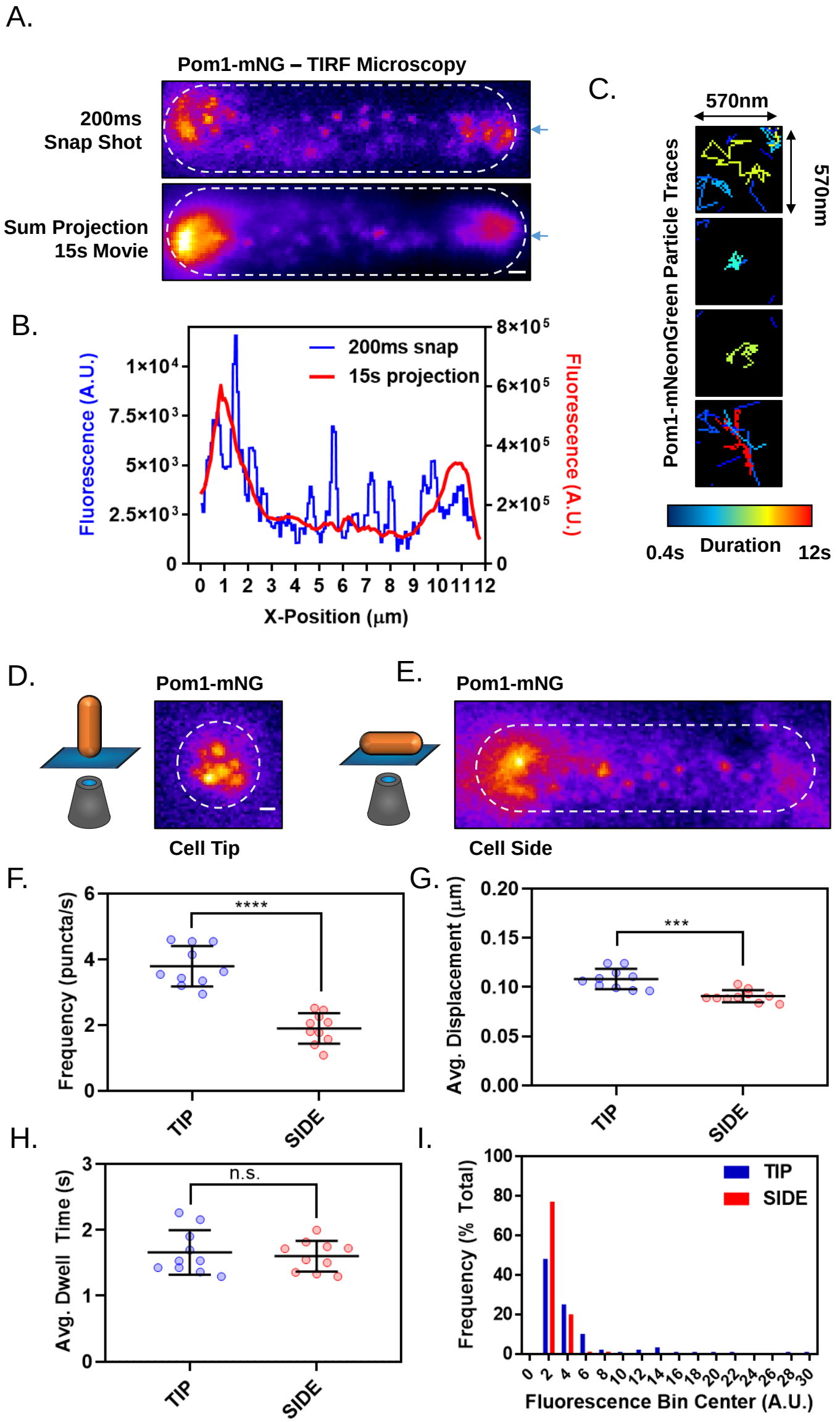
A.
Pom1-mNG – TIRF Microscopy
200ms
Snap Shot
Sum Projection
15s Movie
B.
200ms snap
15s projection
Fluorescence (A.U.)
Fluorescence (A.U.)
X-Position (μm)
C.
570nm
570nm
Pom1-mNeonGreen Particle Traces
0.4s
Duration
12s
D.
Pom1-mNG
Cell Tip
E.
Pom1-mNG
Cell Side
F.
Frequency (puncta/s)
****
TIP
SIDE
G.
Avg. Displacement (μm)
***
TIP
SIDE
H.
Avg. Dwell Time (s)
n.s.
TIP
SIDE
I.
Frequency (% Total)
TIP
SIDE
Fluorescence Bin Center (A.U.)

Figure 1

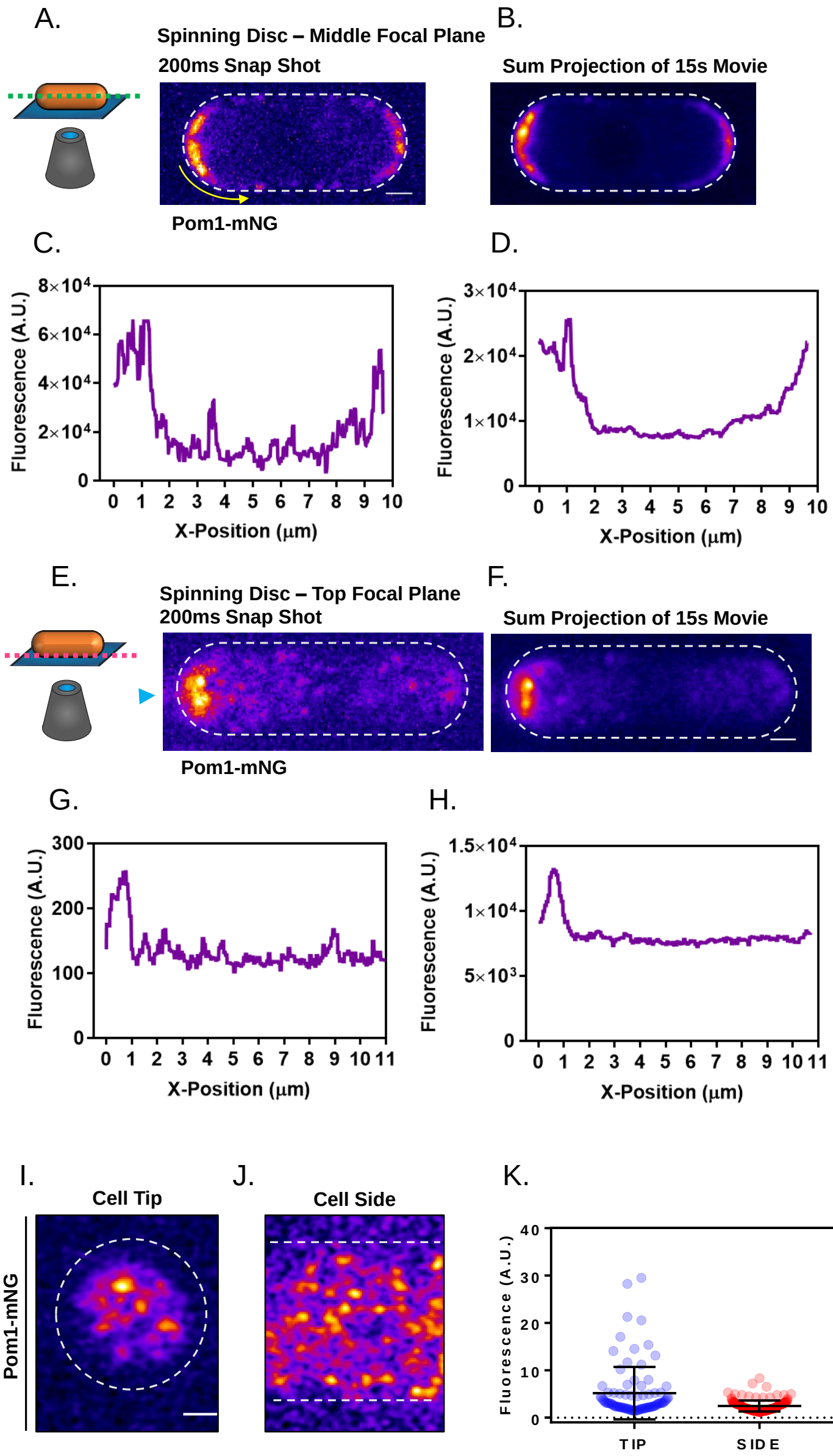

Supplemental Figure 1 in support of Figure 1

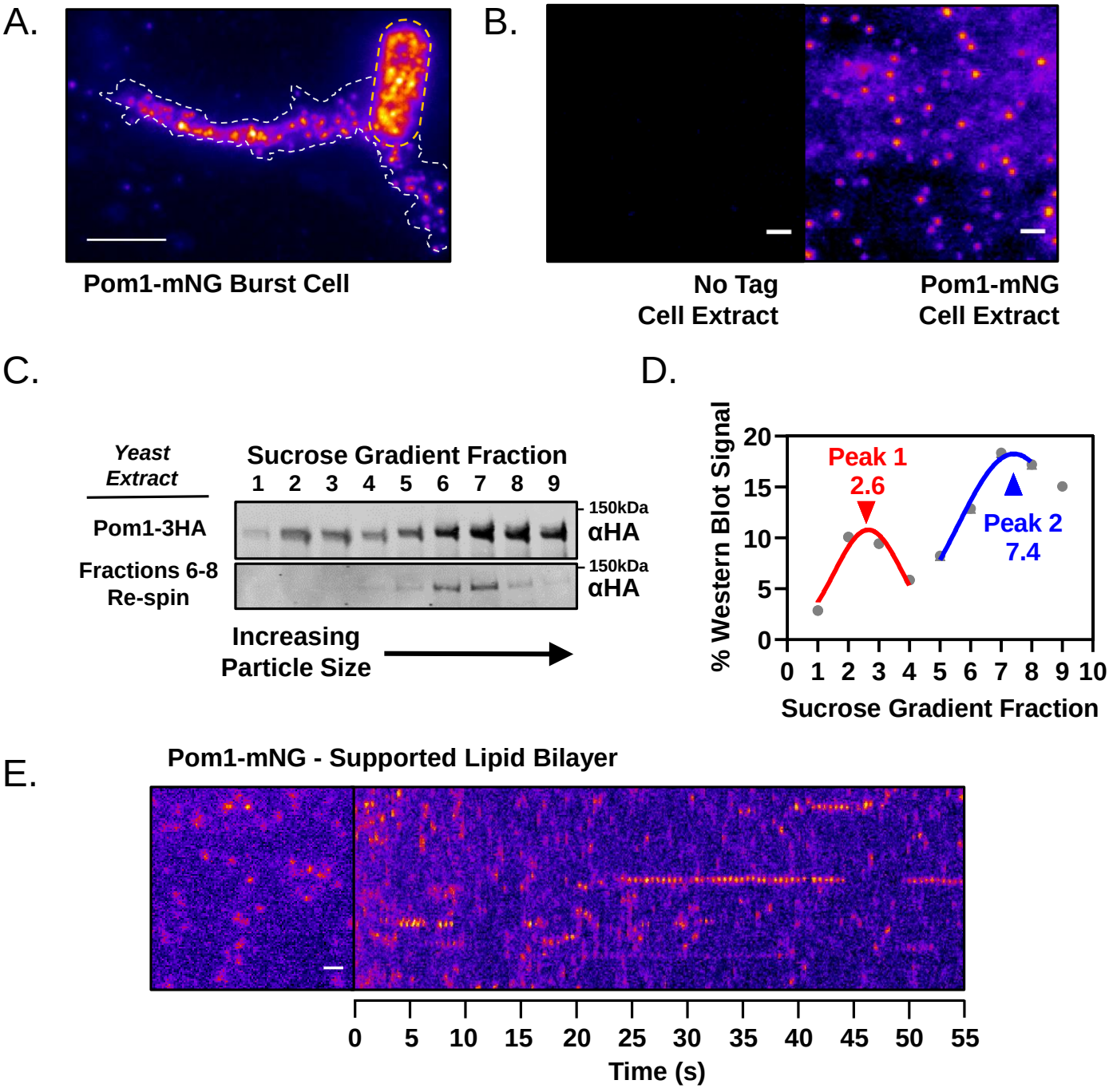
A.
Pom1-mNG Burst Cell
B.
No Tag
Cell Extract
Pom1-mNG
Cell Extract
C.
Yeast
Extract
Sucrose Gradient Fraction
1 2 3 4 5 6 7 8 9
Pom1-3HA
Fractions 6-8
Re-spin
150kDa
αHA
150kDa
αHA
Increasing
Particle Size
D.
% Western Blot Signal
20
15
10
5
0
Peak 1
2.6
Peak 2
7.4
0 1 2 3 4 5 6 7 8 9 10
Sucrose Gradient Fraction
E.
Pom1-mNG - Supported Lipid Bilayer
0 5 10 15 20 25 30 35 40 45 50 55
Time (s)

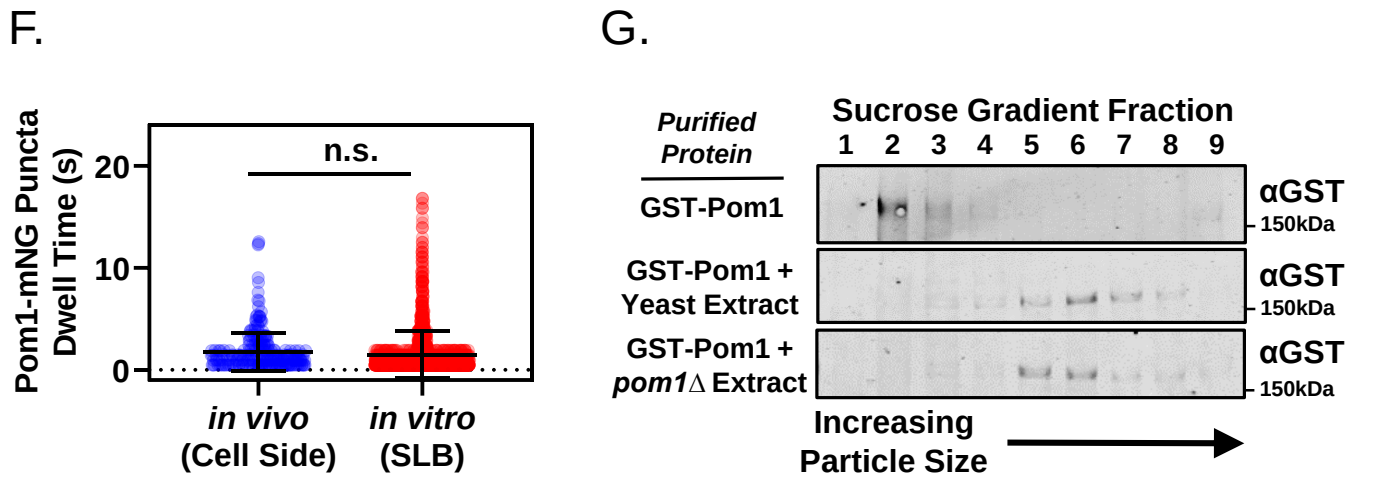
F.
Pom1-mNG Puncta
Dwell Time (s)
20
10
0
n.s.
in vivo
(Cell Side)
in vitro
(SLB)
G.
Purified
Protein
Sucrose Gradient Fraction
1 2 3 4 5 6 7 8 9
GST-Pom1
GST-Pom1 +
Yeast Extract
GST-Pom1 +
pom1Δ Extract
αGST
150kDa
αGST
150kDa
αGST
150kDa
Increasing
Particle Size

Figure 2

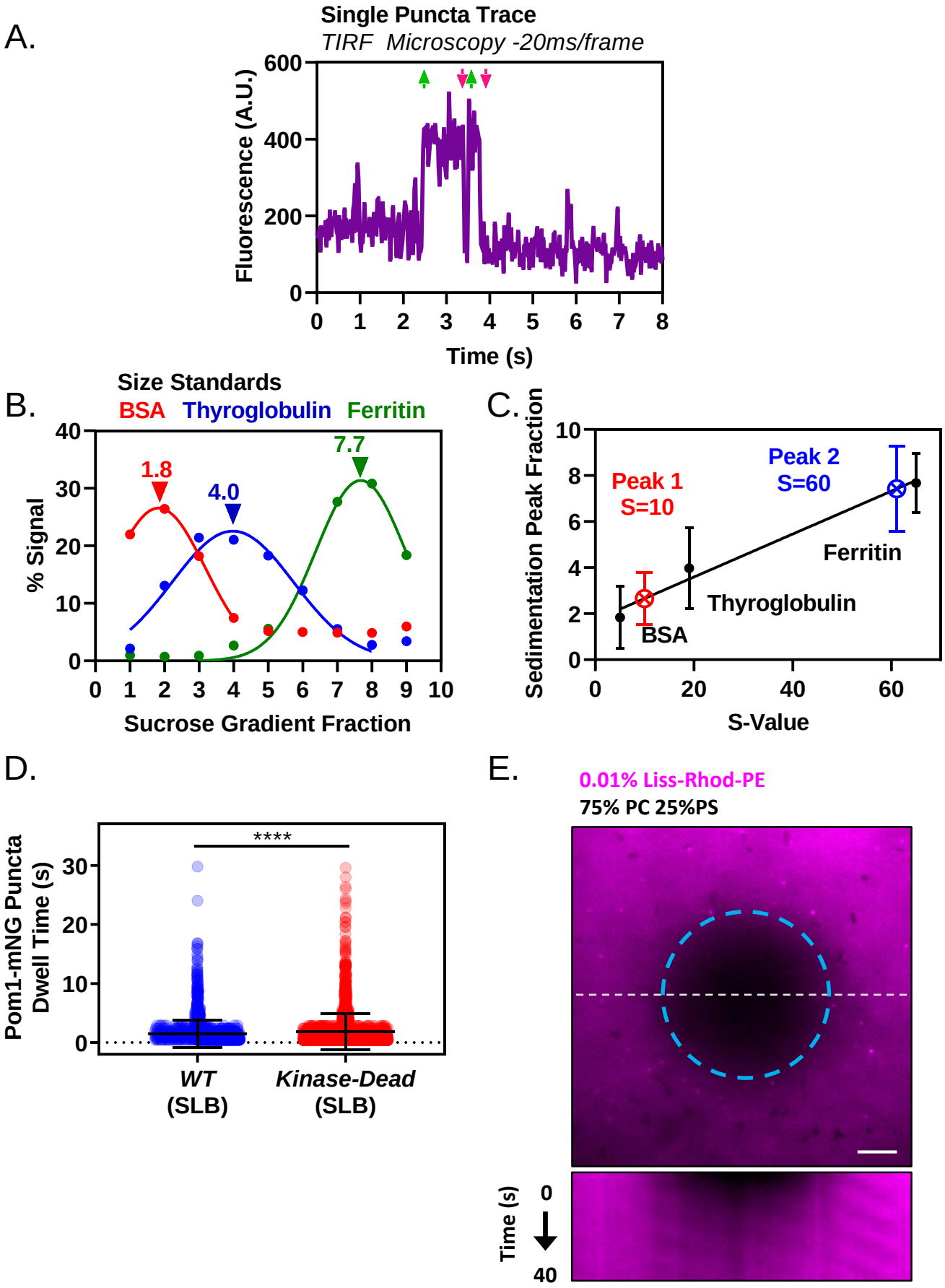

Supplemental Figure 2 in support of Figure 2

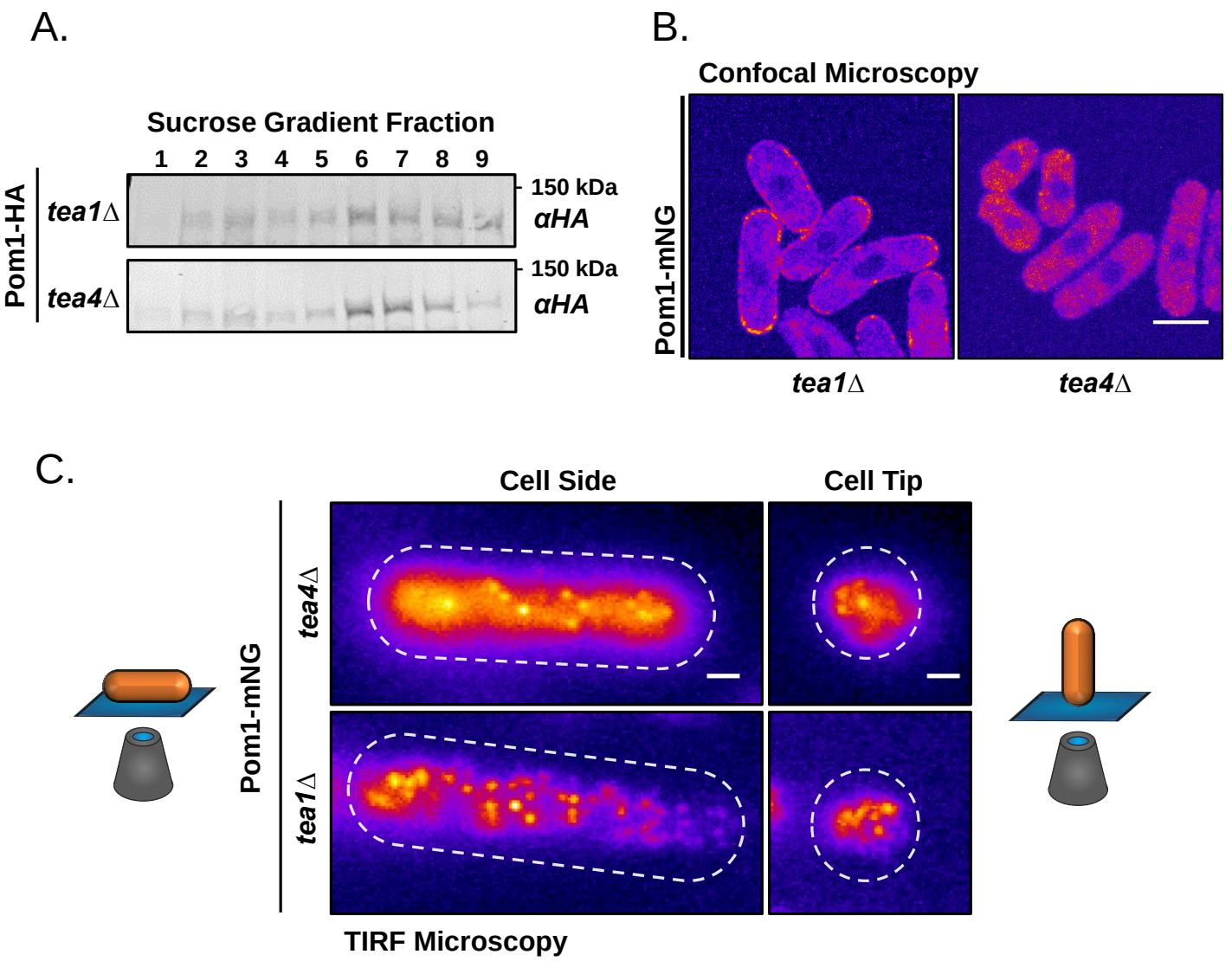
A.
Sucrose Gradient Fraction
1 2 3 4 5 6 7 8 9
Pom1-HA
tea1Δ
tea4Δ
150 kDa
αHA
150 kDa
αHA
B.
Confocal Microscopy
Pom1-mNG
tea1Δ
tea4Δ
C.
Cell Side
Cell Tip
Pom1-mNG
tea4Δ
tea1Δ
TIRF Microscopy

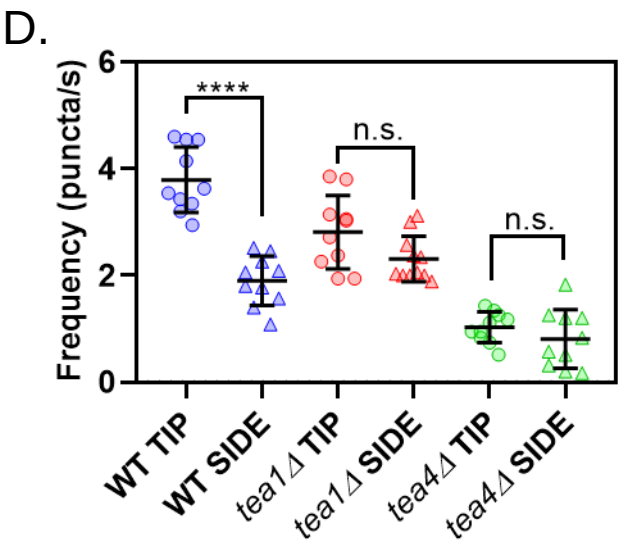
D.
Frequency (puncta/s)
0
2
4
6
****
n.s.
n.s.
WT TIP
WT SIDE
tea1Δ TIP
tea1Δ SIDE
tea4Δ TIP
tea4Δ SIDE

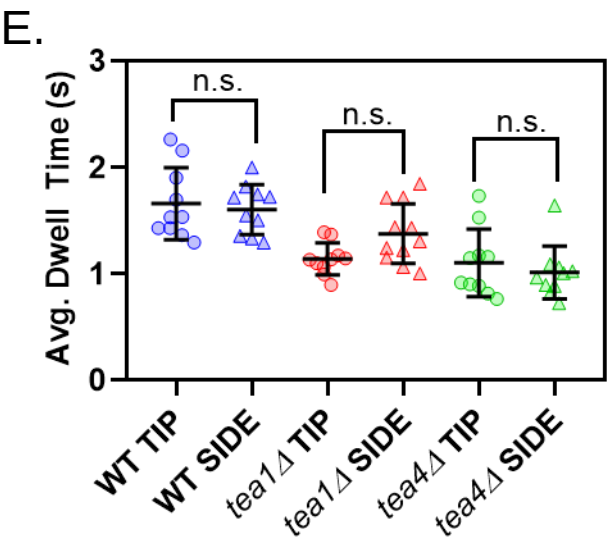
E.
Avg. Dwell Time (s)
0
1
2
3
n.s.
n.s.
n.s.
WT TIP
WT SIDE
tea1Δ TIP
tea1Δ SIDE
tea4Δ TIP
tea4Δ SIDE

Figure 3

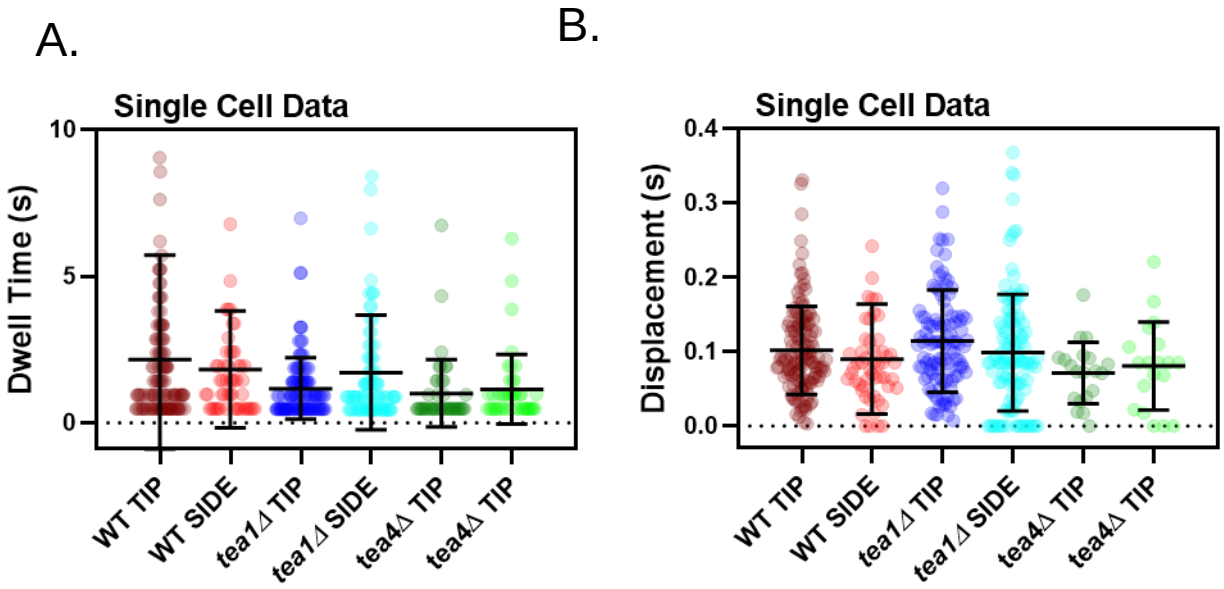

Supplemental Figure 3 in support of Figure 3

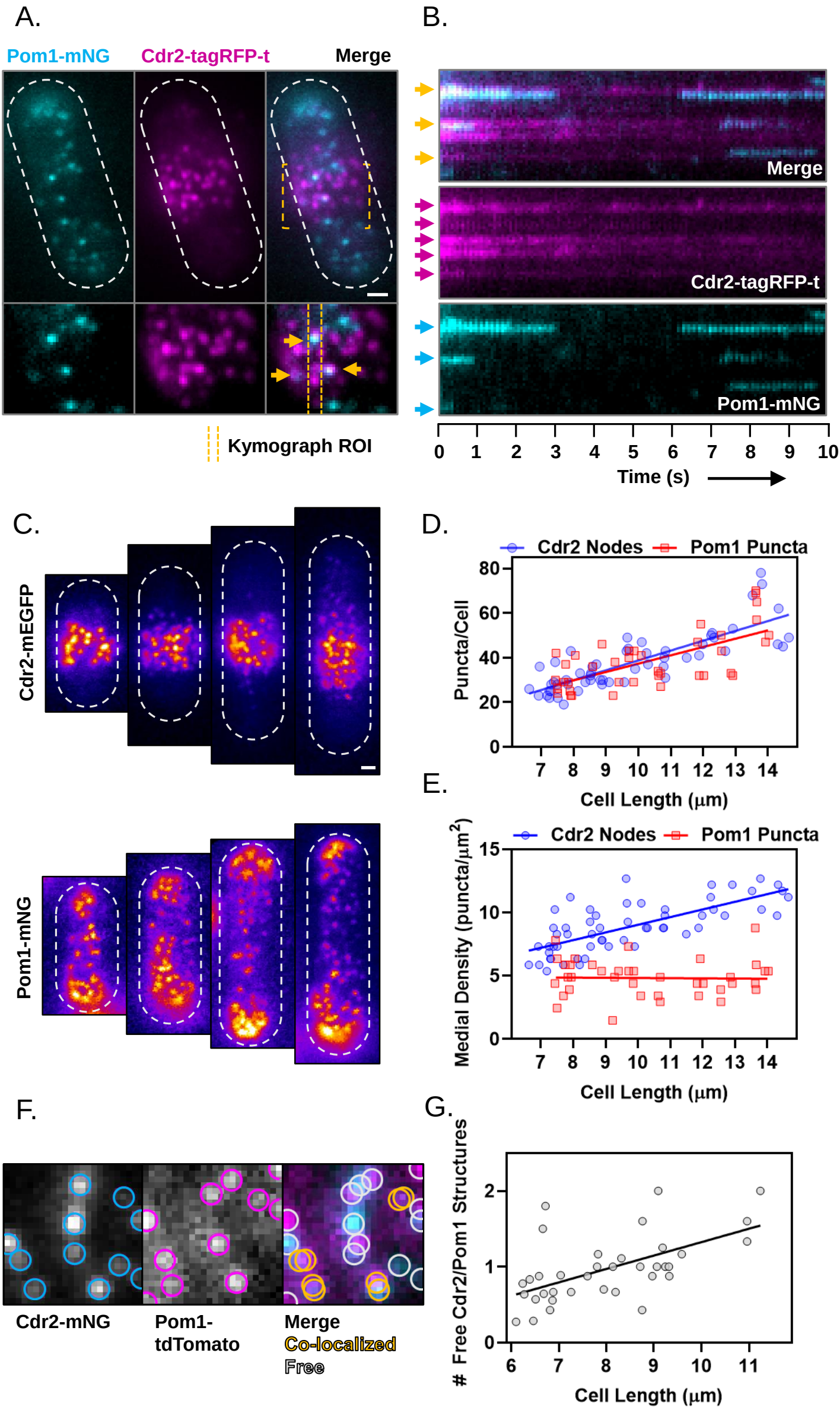
A.
Pom1-mNG
Cdr2-tagRFP-t
Merge
Kymograph ROI
B.
Merge
Cdr2-tagRFP-t
Pom1-mNG
0 1 2 3 4 5 6 7 8 9 10
Time (s)
C.
Cdr2-mEGFP
Pom1-mNG
D.
Cdr2 Nodes
Pom1 Puncta
Puncta/Cell
0 20 40 60 80
7 8 9 10 11 12 13 14
Cell Length (μm)
E.
Cdr2 Nodes
Pom1 Puncta
Medial Density (puncta/μm²)
0 5 10 15
7 8 9 10 11 12 13 14
Cell Length (μm)
F.
Cdr2-mNG
Pom1-tdTomato
Merge
Co-localized
Free
G.
Free Cdr2/Pom1 Structures
0 1 2
6 7 8 9 10 11
Cell Length (μm)

Figure 4

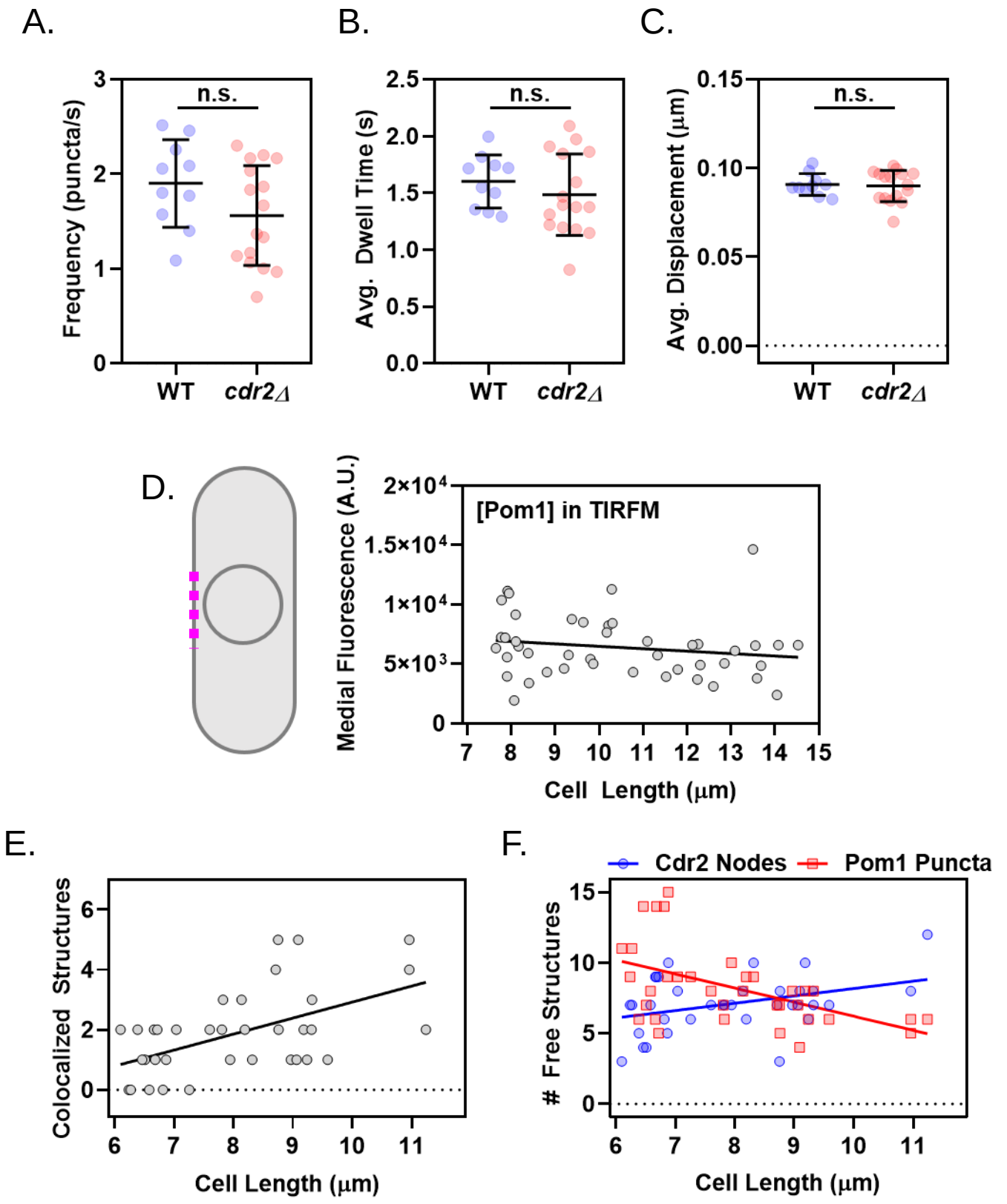

Supplemental Figure 4 in support of Figure 4

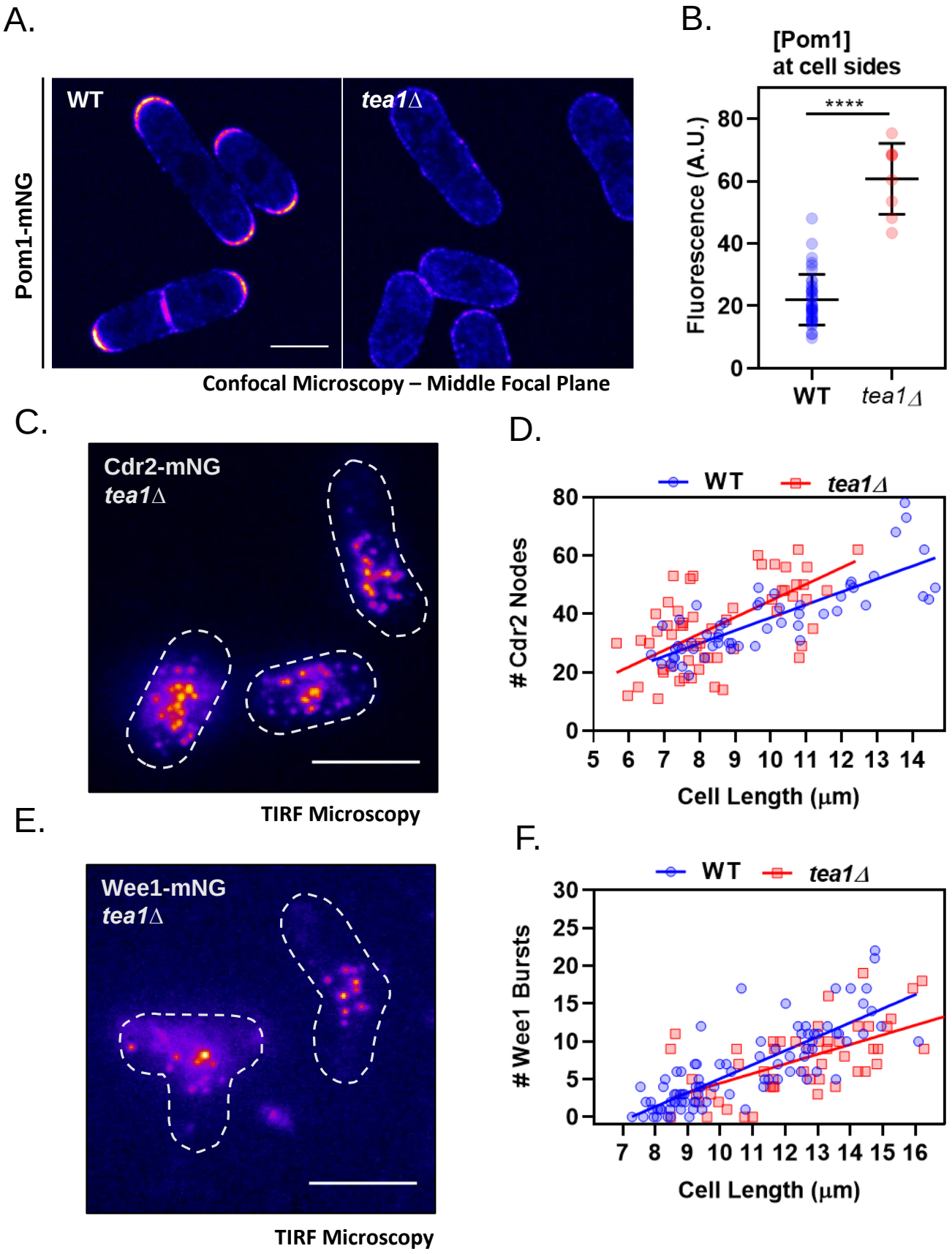
A.
Pom1-mNG
WT
tea1Δ
Confocal Microscopy – Middle Focal Plane
B.
[Pom1]
at cell sides
****
Fluorescence (A.U.)
0
20
40
60
80
WT
tea1Δ
C.
Cdr2-mNG
tea1Δ
TIRF Microscopy
D.
WT
tea1Δ
Cdr2 Nodes
0
20
40
60
80
5 6 7 8 9 10 11 12 13 14
Cell Length (μm)
E.
Wee1-mNG
tea1Δ
TIRF Microscopy
F.
WT
tea1Δ
Wee1 Bursts
0
5
10
15
20
25
30
7 8 9 10 11 12 13 14 15 16
Cell Length (μm)

Figure 5

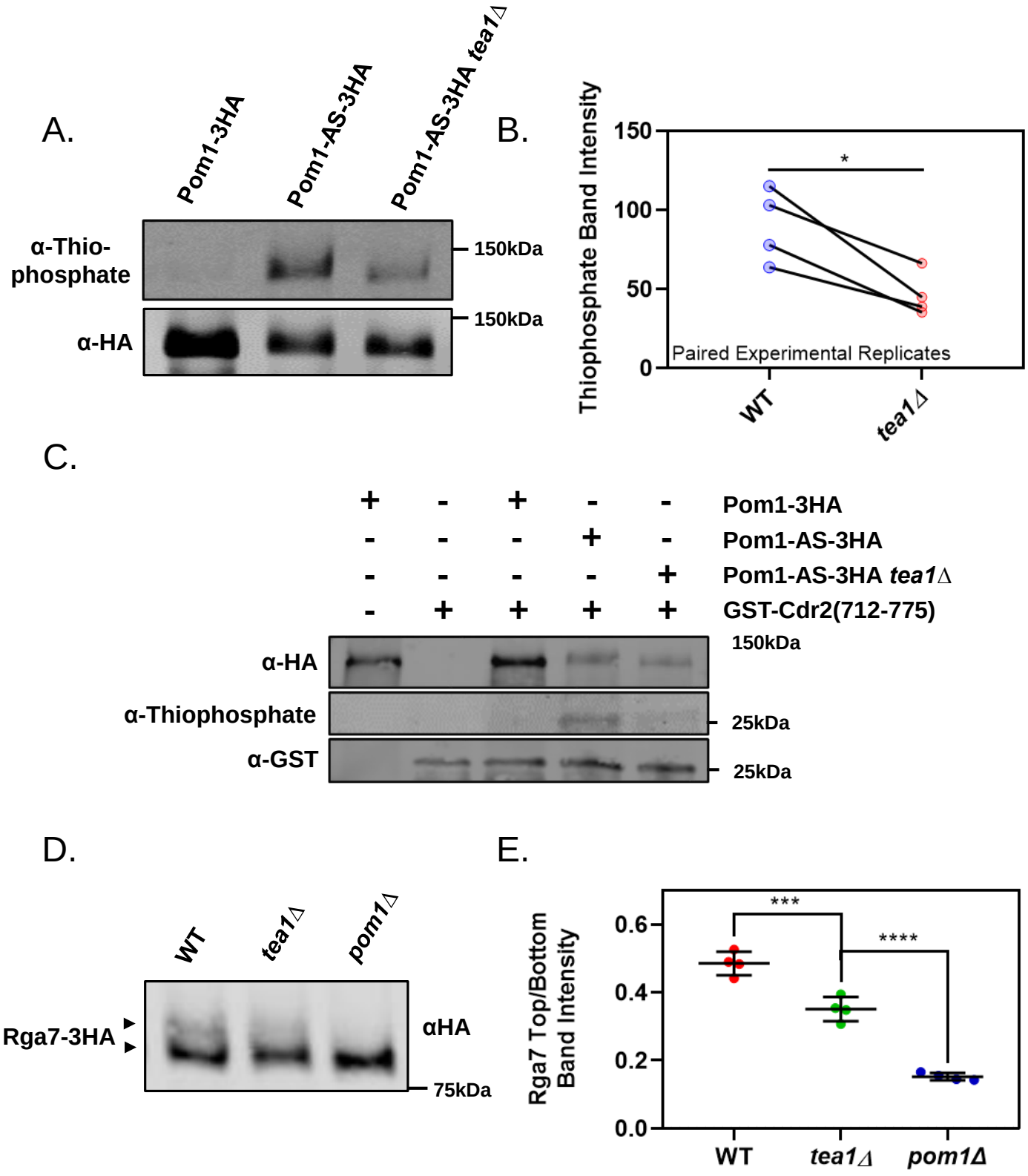

Supplemental Figure 5 in support of Figure 5

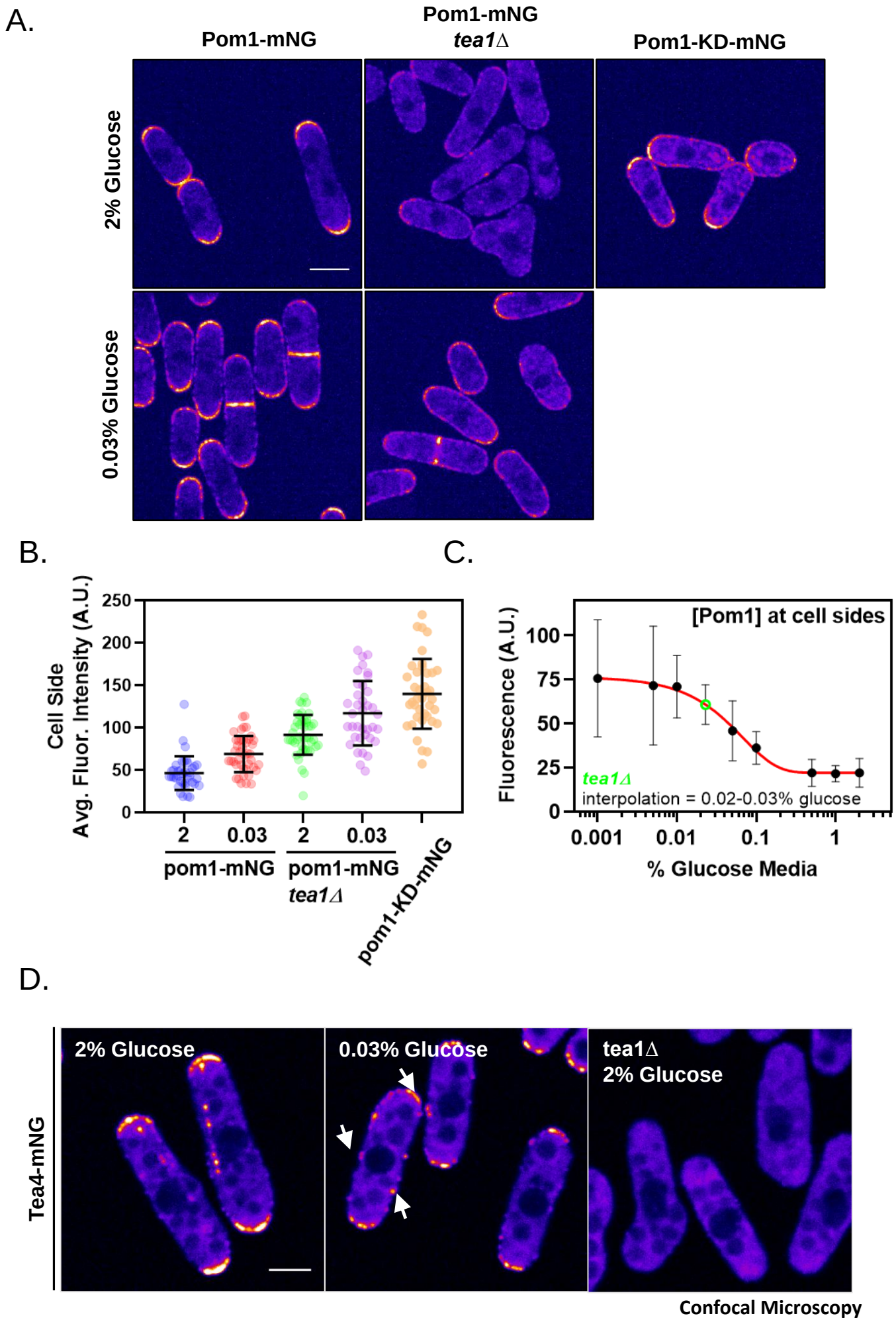

Supplemental Figure 6 in support of Figure 5

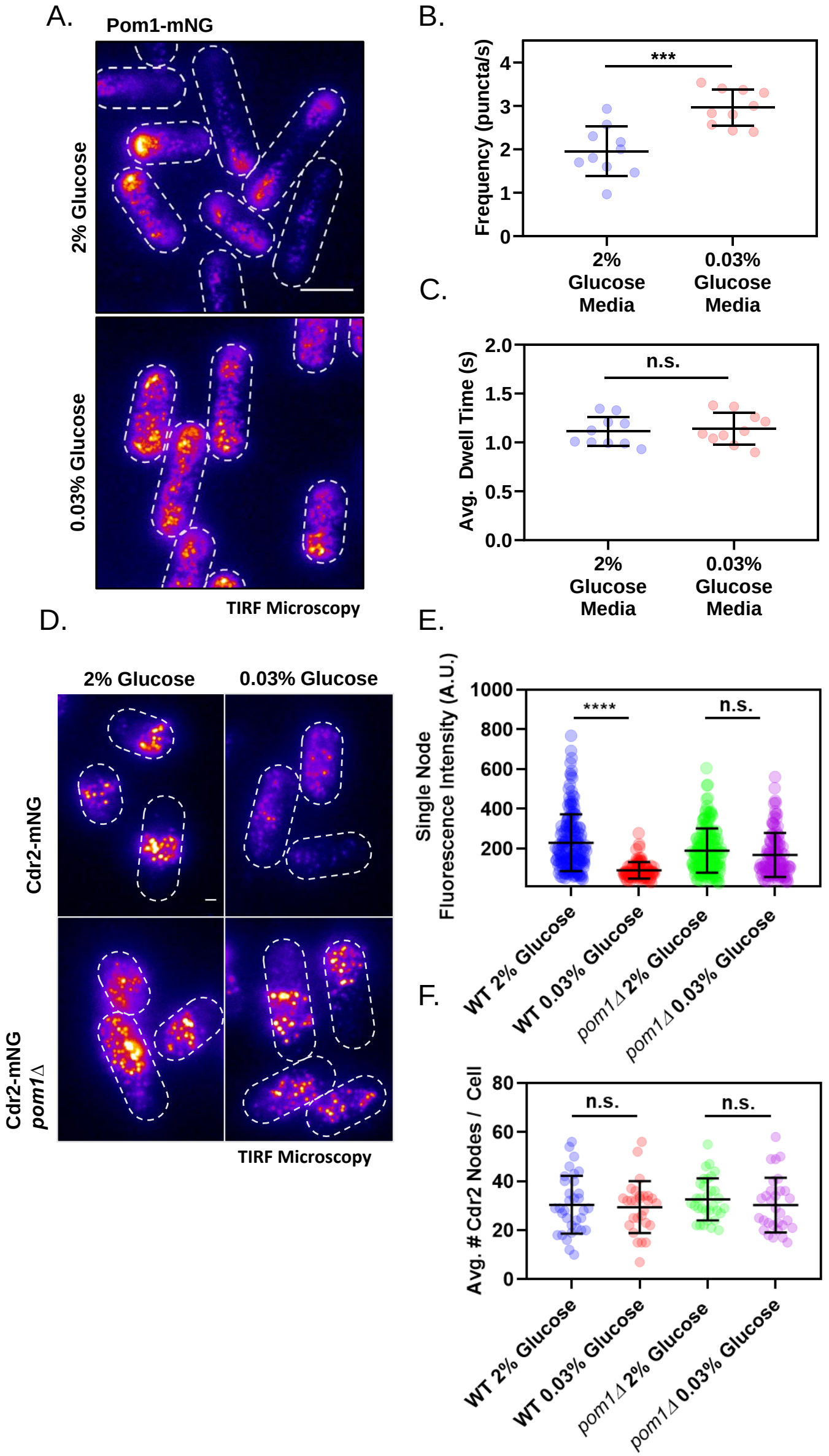
A.
Pom1-mNG
2% Glucose
0.03% Glucose
TIRF Microscopy
B.
Frequency (puncta/s)
***
2% Glucose Media
0.03% Glucose Media
C.
Avg. Dwell Time (s)
n.s.
2% Glucose Media
0.03% Glucose Media
D.
2% Glucose
0.03% Glucose
Cdr2-mNG
Cdr2-mNG pom1Δ
TIRF Microscopy
E.
Single Node Fluorescence Intensity (A.U.)
****
n.s.
WT 2% Glucose
WT 0.03% Glucose
pom1Δ 2% Glucose
pom1Δ 0.03% Glucose
F.
Avg. # Cdr2 Nodes / Cell
n.s.
n.s.
WT 2% Glucose
WT 0.03% Glucose
pom1Δ 2% Glucose
pom1Δ 0.03% Glucose

Figure 6

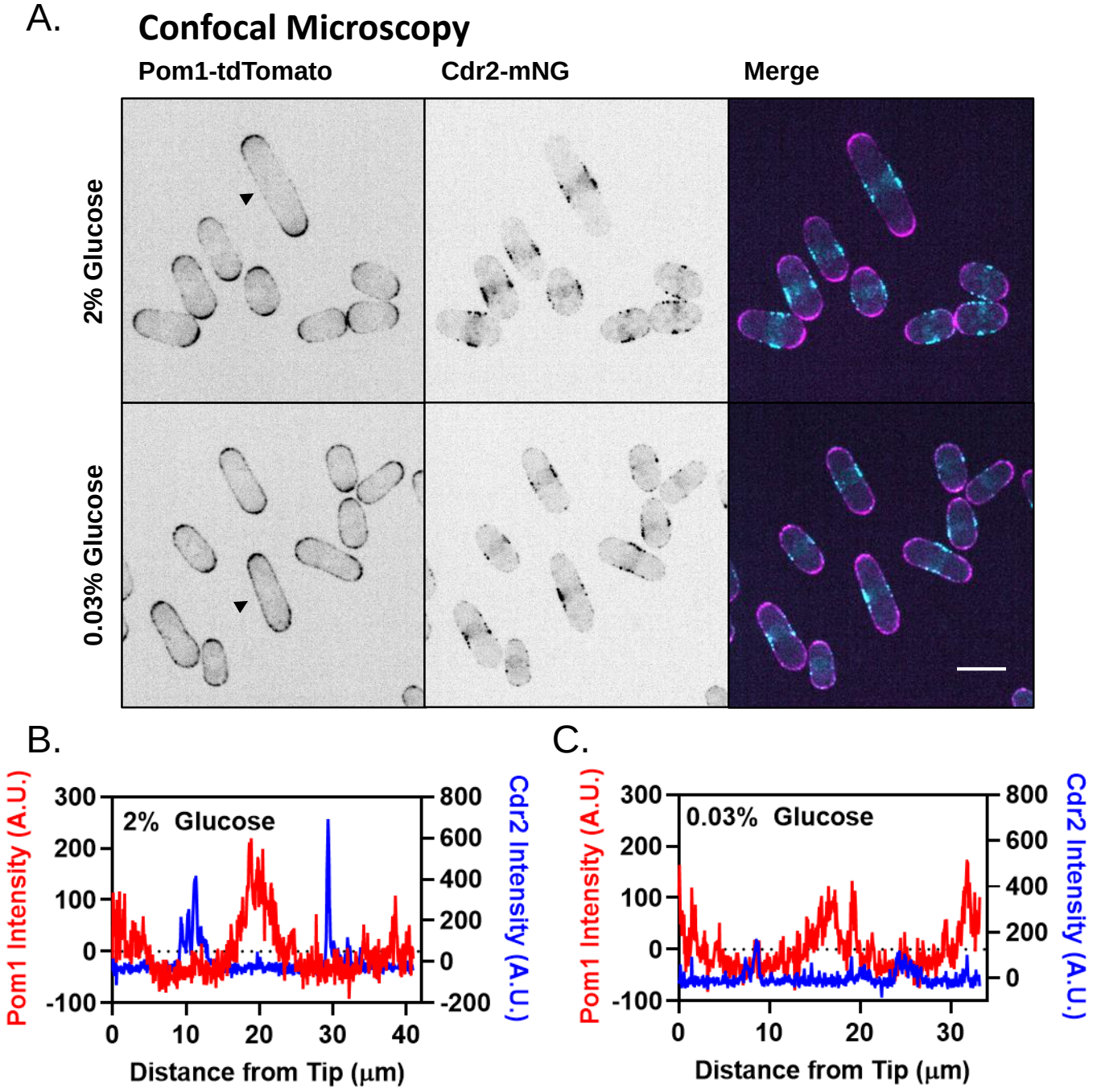

Supplemental Figure 7 in support of Figure 6

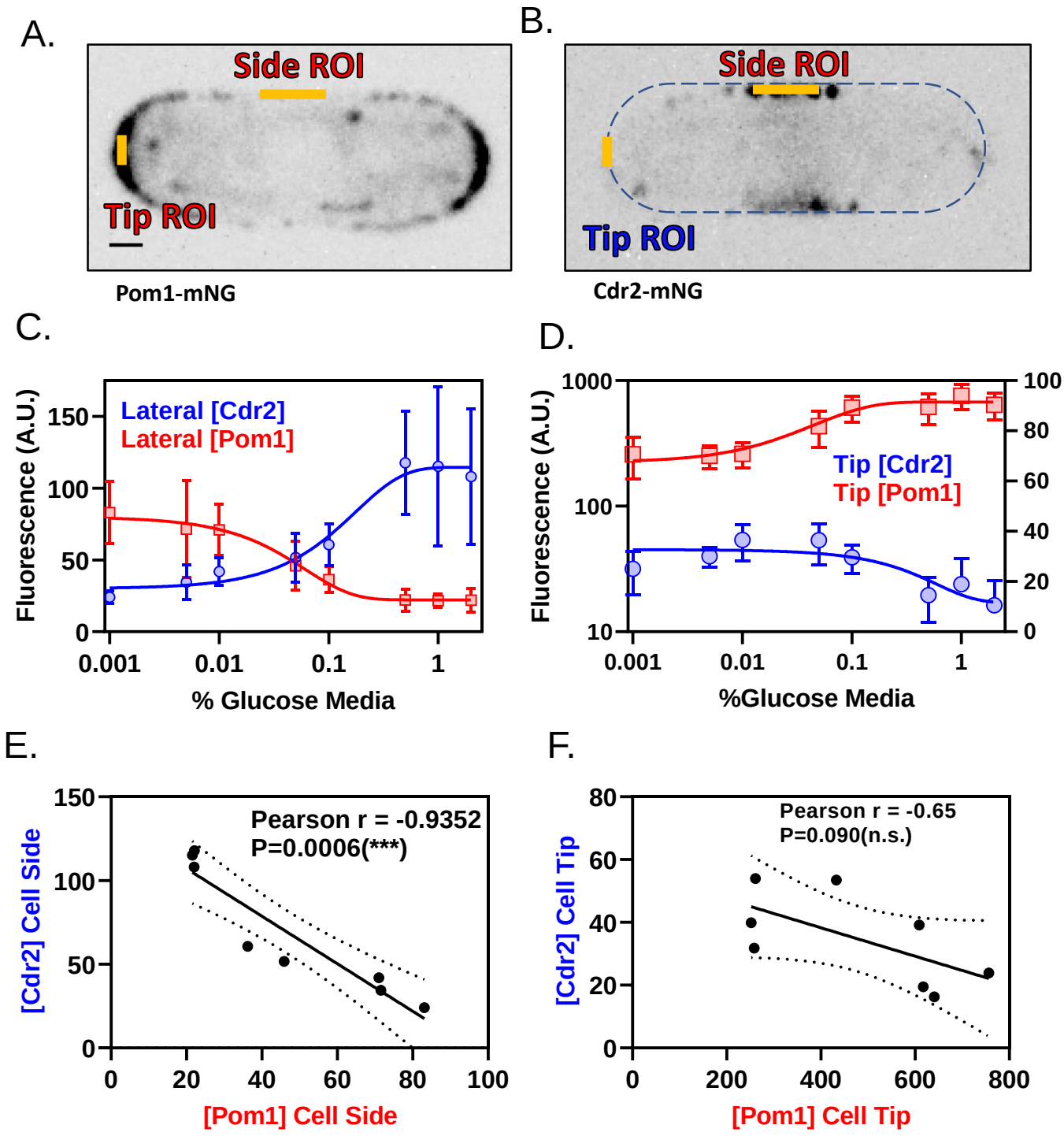
A.
Side ROI
Tip ROI
Pom1-mNG
B.
Side ROI
Tip ROI
Cdr2-mNG
C.
Lateral [Cdr2]
Lateral [Pom1]
Fluorescence (A.U.)
150
100
50
0
0.001
0.01
0.1
1
% Glucose Media
D.
Tip [Cdr2]
Tip [Pom1]
Fluorescence (A.U.)
1000
100
10
100
80
60
40
20
0
0.001
0.01
0.1
1
%Glucose Media
E.
Pearson r = -0.9352
P=0.0006(***)
[Cdr2] Cell Side
150
100
50
0
0
20
40
60
80
100
[Pom1] Cell Side
F.
Pearson r = -0.65
P=0.090(n.s.)
[Cdr2] Cell Tip
80
60
40
20
0
0
200
400
600
800
[Pom1] Cell Tip

Figure 7

A.

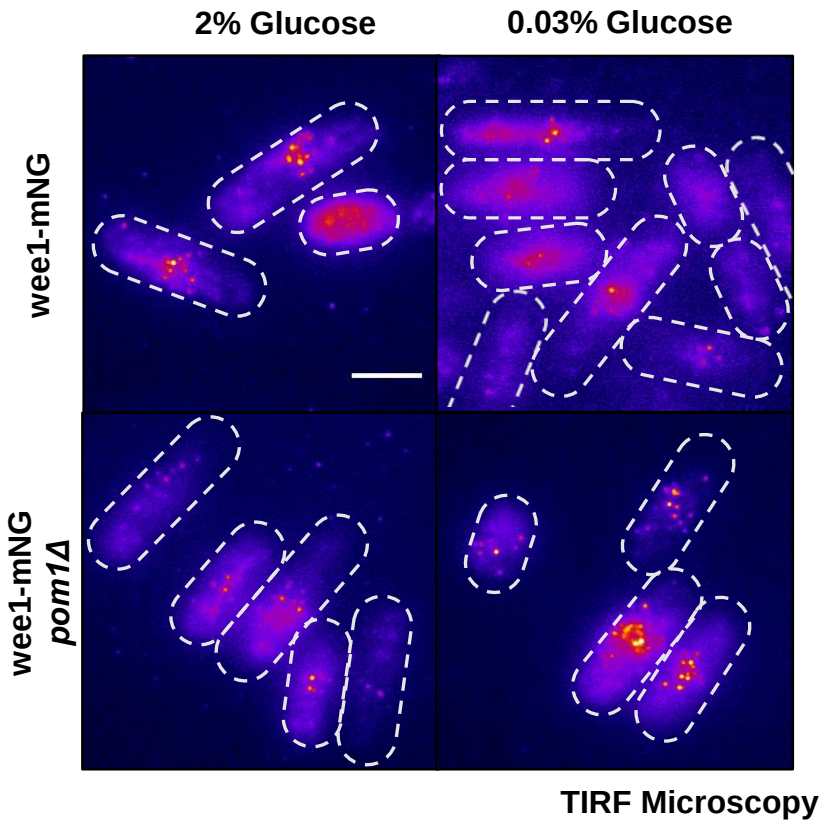

B. C.

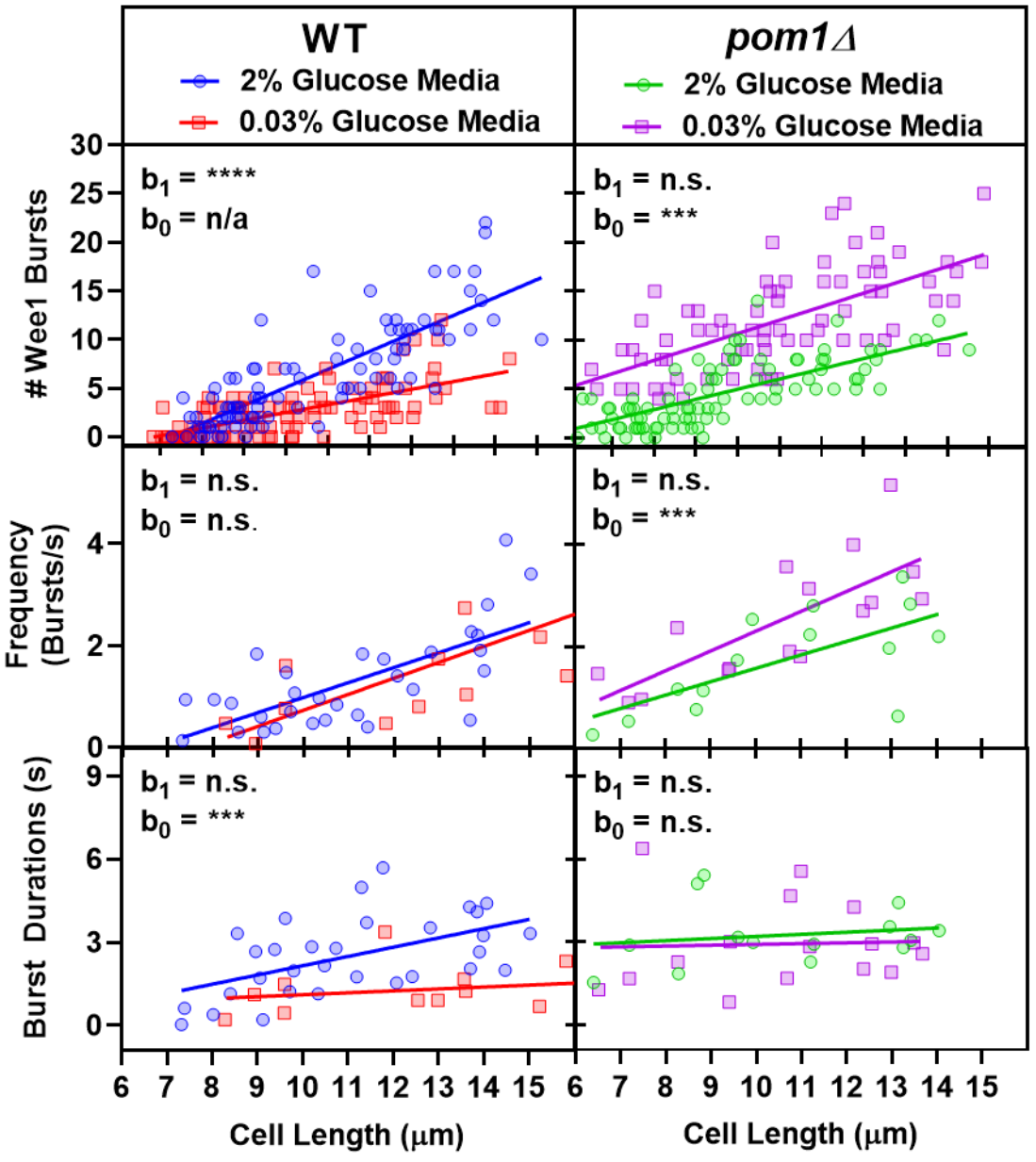

D.

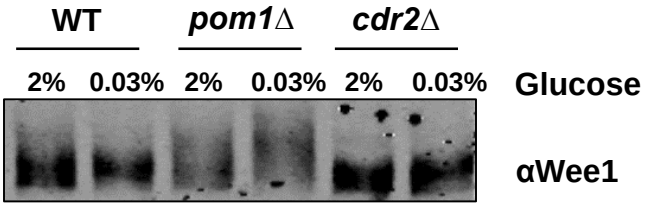

Figure 8

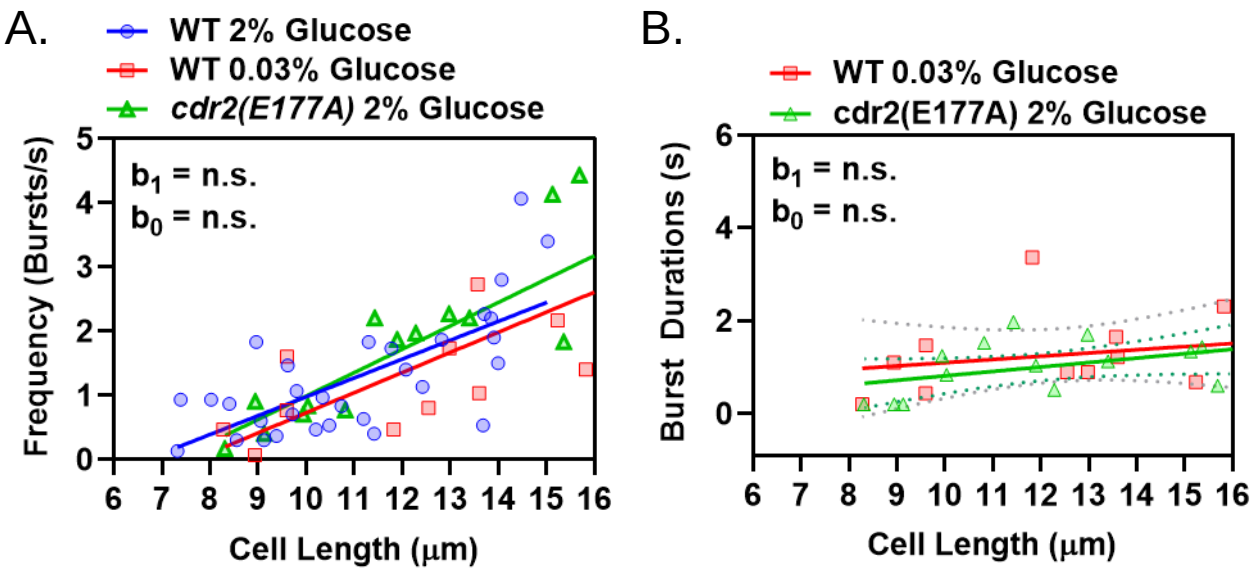

Supplemental Figure 8 in support of Figure 8

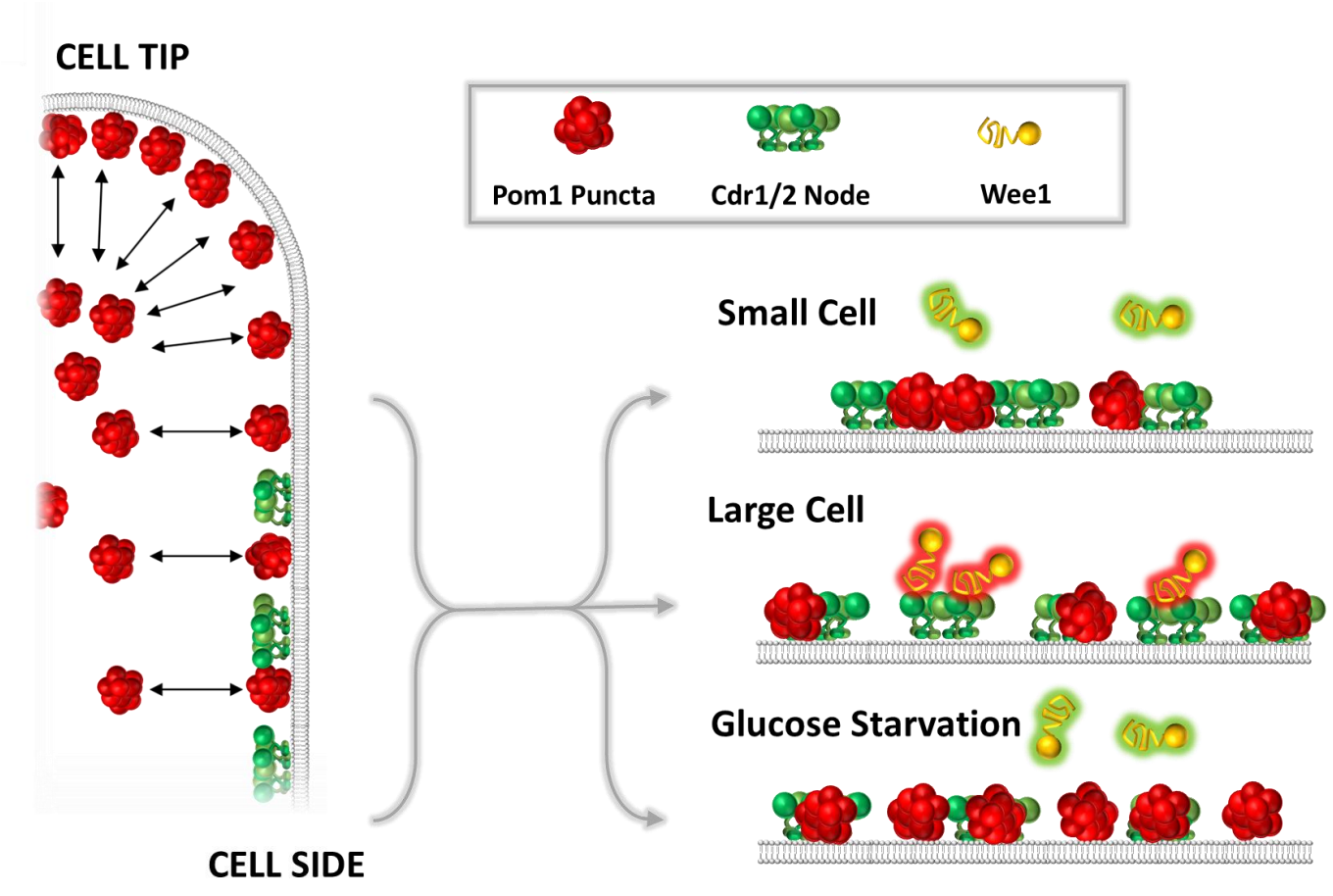
CELL TIP
Pom1 Puncta
Cdr1/2 Node
Wee1
Small Cell
Large Cell
Glucose Starvation
CELL SIDE

Figure 9

Strains used in this study:			
Strain	**Genotype**	**Origin**	**Figure**
JM4496	*pom1-yomNeonGreen::hphR*	This Study	1A-I, S1A-K, 2A-B,E-F, S2A,D, 3D-F, S3A-B, 4C-E, S4A-D, 5A-B, S6A-C, 6A-C, 7A,C-F
JM797	*pom1-3HA::hphR ura4-D18 leu1-32 h+*	PN948 (Paul Nurse Lab)	2C-D,G, S5A,C
JM966	*pom1Δ::natR h-*	Lab Stock	2G, 8D
JM5412	*pom1-m2-yomNeonGreen::hphR ura4-D18 leu1-32 h-*	This Study	S2D, S6A-B
JM5414	*pom1-3HA::hphR tea1Δ::ura4+ ura4-D18*	This Study	3A
JM5415	*pom1-3HA::hphR tea4Δ::kanMX6*	This Study	3A
JM4792	*pom1-yomNeonGreen::hphR tea1Δ::kanMX6*	This Study	3B-F, S3A-B, 5A-B, S6A-C
JM4791	*pom1-yomNeonGreen::hphR tea4Δ::kanMX6*	This Study	3B-F, S3A-B
JM5373	*pom1-yomNeonGreen::hphR cdr2-tagRFP-t::hphR*	This Study	4A-B
JM4493	*cdr2-yomNeonGreen::hphR h-*	Lab Stock	4C-E, 6D-F, 7B-F
JM4525	*wee1-yomNeonGreen::hph cdr2Δ::natR*	Lab Stock	S4A-C
JM5135	*cdr2-yomNeonGreen::hphR pom1-tdTomato::natR*	This Study	4F-G, S4E-F, S7A-C
JM5374	*cdr2-yomNeonGreen::hphR tea1Δ::kanMX6*	This Study	5C-D
JM5372	*wee1-yomNeonGreen::hphR tea1Δ::kanMX6*	This Study	5E-F
JM2209	*rga7-3HA::hphR h-*	Lab Stock	S5D-E
JM5612	*rga7-3HA::hphR tea1Δ::kanMX6*	This Study	S5D-E
JM2210	*rga7-3HA::hphR pom1Δ::kanMX6*	Lab Stock	S5D-E
JM4211	*pom1-as-3HA::hphR*	Lab Stock	S5A-C
JM5565	*pom1-as-3HA::hphR tea1Δ::kanMX6 ura4-D18*	This Study	S5A-C
JM5132	*tea4-yomNeonGreen::hphR h-*	This Study	S6D
JM5733	*tea4-yomNeonGreen::hphR tea1Δ::kanMX6*	This Study	S6D
JM5359	*cdr2-yomNeonGreen::hphR pom1Δ::natR*	This Study	6D-F
JM4495	*wee1-yomNeonGreen::hphR h-*	Lab Stock	8A-B, S8A-B
JM4527	*wee1-yomNeonGreen::hphR pom1Δ::kanMX6*	Lab Stock	8A,C
JM366	*972 h-*	PN1 (Paul Nurse lab)	8D
JM600	*cdr2Δ::natR ura4-D18 leu1-32 h+*	Lab Stock	8D
JM4578	*wee1-yomNeonGreen::hphR cdr2(E177A)*	Lab Stock	S8A-B

Supplemental Table 1